
Co-Active Subspace Methods for the Joint Analysis of Adjacent Computer Models

Kellin N. Rumsey¹

Statistical Sciences
Los Alamos National Laboratory
Los Alamos, NM 87545
knrumsey@lanl.gov

Zachary K. Hardy

X Theoretical Design Division
Los Alamos National Laboratory
Los Alamos, NM 87545
zhardy@lanl.gov

Cory Ahrens

X Theoretical Design Division
Los Alamos National Laboratory
Los Alamos, NM 87545
cdahrens@lanl.gov

Scott Vander Wiel

Statistical Sciences
Los Alamos National Laboratory
Los Alamos, NM 87545
scottv@lanl.gov

Abstract

Active subspace (AS) methods are a valuable tool for understanding the relationship between the inputs and outputs of a Physics simulation. In this paper, an elegant generalization of the traditional ASM is developed to assess the co-activity of two computer models. This generalization, which we refer to as a Co-Active Subspace (Co-AS) Method, allows for the joint analysis of two or more computer models allowing for thorough exploration of the alignment (or non-alignment) of the respective gradient spaces. We define co-active directions, co-sensitivity indices, and a scalar “concordance” metric (and complementary “discordance” pseudo-metric) and we demonstrate that these are powerful tools for understanding the behavior of a class of computer models, especially when used to supplement traditional AS analysis. Details for efficient estimation of the Co-AS and an accompanying R package (`concordance`) are provided. Practical application is demonstrated through analyzing a set of simulated rate stick experiments for PBX 9501, a high explosive, offering insights into complex model dynamics.

1 Introduction

In modern physical science, complex real-world systems are often modeled based on the current understanding of the physics governing the problem. These computer models (also called simulators) have proven to be valuable tools for advancing scientific knowledge. It is a common practice to consider a class of two or more computer models that endeavor to simulate the same (or similar) physical phenomena; we refer to these computer models as *adjacent*. Examples include: (i) computer models calibrated via distinct methods and/or data sources (Kennedy & O’Hagan 2001, Michelsen et al. 2007), (ii) computer models approximated with different fidelities or emulated using different methods (Peherstorfer et al. 2018, Zhang & Zhang 2020, Gramacy 2020), (iii) computer models grounded in competing theories of the underlying physics (Bernstein et al. 2019, Finnegan et al. 2022, Yannotty et al. 2024), and (iv) computer models describing neighboring physical processes. Within this context, the central focus revolves around comprehending the discrepancies and commonalities among these models, determining the point at which their similarity deems them as neighbors. We also seek to understand how the common inputs jointly affect these simulators.

For a single function (computer model) of interest, active subspace methods (ASM) (Constantine 2015) have emerged as a popular tool for exploring the intricate relationship between inputs and outputs within a physics simulator (Lukaczyk et al. 2014, Constantine et al. 2015, Constantine & Doostan 2017, Seshadri et al. 2018, Tezzele et al. 2018, Ji et al. 2019, Batta et al. 2021). ASM involves identifying a set of orthogonal directions within the input space that produce the largest changes in the response. In the case of multiple computer models (or equivalently, a vector-valued function), Zahm et al. (2020) and Ji et al. (2018) propose methods for discovering a so-called *shared* active subspace. These approaches focus on finding a single subspace upon which all functions are simultaneously active. Commonly, the approach of Zahm et al. (2020) reduces to finding a key matrix C_k for each function of interest and working with their sum, $\mathbf{H} = \sum_{k=1}^K C_k$. This approach has proven to be highly successful in theory and in practice.

In addition to active subspace based methods, the literature on multivariate sufficient dimension reduction (MSDR) is relevant to this discussion (Hsing 1999, Setodji & Cook 2004, Li et al. 2008, Cook 2022). SDR methods, like sliced inverse regression (Li 1991), attempt to find subspaces such that the conditional distribution of the model output given the inputs varies only within the subspace. The smallest such subspace is called the “central subspace” and is the target of SDR. The central subspace can be challenging to find, and most methods rely on easier to find yet related subspaces (e.g., the central mean subspace). MSDR methods generalize these approaches to multiple functions (see (Dong et al. 2023) for a review).

Although closely related, the approach outlined in this manuscript differs from previous work in several important ways. First of all, our primary interest is not in finding a single active subspace which is effective for all functions (although it can be useful here). Rather, we are interested in understanding the complex relationship between two adjacent computer models and determining the directions within the input space along which each model’s gradients are well-aligned. In particular, we introduce co-active directions, co-sensitivity indices, and a metric called *concordance* that supplies a univariate measure of the alignment between the gradient spaces of two functions. So while previous work focuses on studying a class of K functions, our methods are tailor-made for the pairwise study of two functions at a time.

The motivation for this extension stemmed from the real-world challenge of leveraging existing data from one physical system to aid in the design of a similar, but not identical, new system. Standard engineering practice dictates that comprehensive full-system tests are essential to ensure the functionality of a new design Buede & Miller (2016). However, the unique context of our problem precludes such exhaustive testing, necessitating alternative means of design assurance. This is where the concept of co-activity comes into play.

In Section 2, we provide a mathematical description of the problem and state several key questions which are of scientific interest. We also motivate the problem by describing rate stick experiment simulations with PBX 9501, a commonly studied high explosive (HE), and provide a brief review of traditional AS methods. Mathematical details and definitions for the Co-Active Subspace (Co-AS) method is given in Section 3, and is illustrated using a simple class of multinomial computer models. We also provide details for efficiently estimating the Co-AS and refer the reader to the accompanying R package (available at github.com/knrumsey/concordance). Section 4 gives a sample analysis using the rate stick experiment simulations on PBX 9501, and concluding remarks are provided in Section 5.

2 Background and Motivation

2.1 Adjacent Computer Models

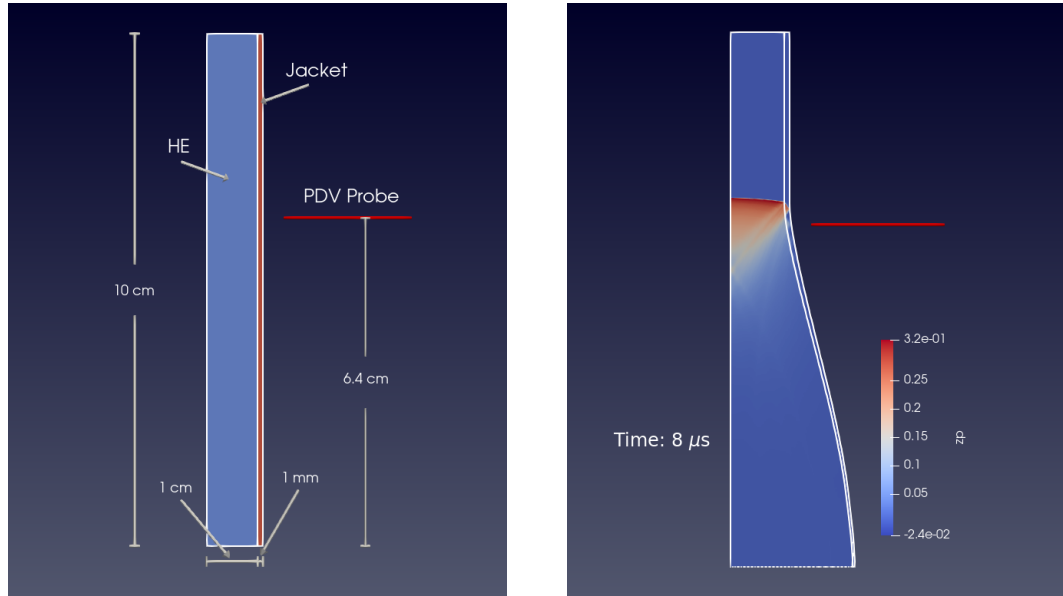
If computer models f_1 and f_2 share a common set of inputs $\boldsymbol{x} \in \mathcal{X} \subset \mathbb{R}^p$ and they describe the same (or similar) physical process, then we say that f_1 and f_2 are *adjacent* computer models. Any prior information over the inputs \boldsymbol{x} , represented by the density $\pi(\boldsymbol{x})$, must be shared by all functions. The second condition, that the functions must describe the same process, is difficult to pin down precisely. To clarify this concept, we give three concrete examples.

- *Models with Different Fidelity or Resolution:* Consider a computer model which is characterized by a partial differential equation (PDE) with uncertain inputs \boldsymbol{x} . Often, this PDE must be solved numerically, such as via finite differences. Representing a highly accuracy solution, $f_1(\boldsymbol{x})$, is solved on a high-resolution grid and may be expensive to run. Alternatively, $f_2(\boldsymbol{x})$ is a “low-fidelity” solution if it is solved over a coarse grid, perhaps sacrificing some accuracy for faster computation time (Peherstorfer et al. 2018).
- *Differing Physics:* Variations of a computer model can arise when there are competing theories of the physics which govern the underlying process. For instance, Bernstein et al. (2019) consider a large class of computer models which attempt to predict material flow strength. The models differ only in the form and parameters of a material strength model. The relative accuracy of each model may depend on the material being modeled or on the region of input-space (i.e. pressure/temperature) of interest.
- *Neighboring Systems:* Rather than modeling the exact same system, some model classes may attempt to explain/predict similar systems. In this scenario, one would seek to gain insight into an “un-trusted” model by comparing its behaviors to a “trusted” model, potentially validated against experimental data. A detailed example of this case is given in Section 2.2.

We are often interested in studying a class models, denoted $\mathcal{F} = \{f_1, f_2, \dots, f_K\}$, in which all members of the class are pairwise adjacent. In these settings, there are a number of important questions a practitioner may seek to answer, such as

- Q1. How similar are models f_k and f_ℓ with respect to the inputs \boldsymbol{x} ? In particular, do they respond similarly to perturbations? That is, are their active subspaces well-aligned?
- Q2. Can we partition (or cluster) the functions into groups of “neighboring” models?
- Q3. Which inputs are the most “important” simultaneously for functions f_k and f_ℓ ? How does this compare to the effect of these inputs on each function independently?
- Q4. Can we produce a low dimensional representation of \boldsymbol{x} that can be used to capture variability in both f_k and f_ℓ simultaneously?

In this manuscript, we develop and present approaches which seek to answer these questions effectively. Q1 is discussed in Section 3.1, where Equation (10) defines a scalar-value measure called *concordance*.



(a) The schematic for the rate stick experiment. (b) A depiction of the rate stick experiment at the time the PDV velocity reading is taken.

Figure 1

Q2 is closely related to Q1 and our proposed solution (using the notion of *discordance*, Equation (11)) is demonstrated in Figure 6. We define *co-activity scores* in Equations (20) and (21) which can be used (in addition the *contribution vectors*, Equation (18)) to address Q3, as demonstrated for PBX9501 in Section 4.1. Finally, Q4 is not the primary focus of this work, but it is an important question which many other authors have addressed. *Co-active directions* are defined in Equation (16) and can sometimes be useful for this purpose. An example of this approach, along with a comparison to the method of Zahm et al. (2020), is given in Section 4.2.

2.2 Rate Stick Experiments for PBX 9501

In this section, we describe a series of computer experiments conducted for the PBX 9501 high explosive (HE) and discuss its connection to the present framework. Rate stick experiments, or cylinder tests, are often used to characterize the performance of an HE. These experiments are carried out by detonating a cylindrical stick of HE surrounded by a metal jacket. Photon Doppler Velocimetry (PDV) diagnostics are used to measure the liner velocity at various axial locations to track the progress of the detonation (see Figure 1). The collected PDV data can then be used to infer properties of the HE detonation process. In these cases, PDV data far enough away from the detonation point for the detonation front to burn in a steady manner are desirable.

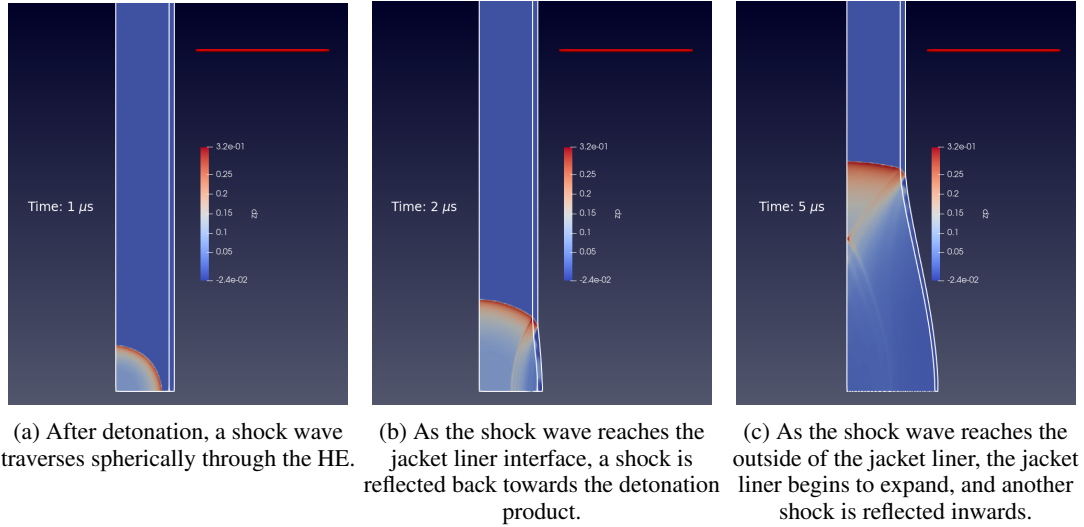


Figure 2: A depiction of the complicated non-linear dynamics governing the rate stick experiment.

The rate stick experiment begins with a detonator firing at the center of the bottom face of a cylinder of HE, causing a shock wave to propagate spherically through the HE (Figure 2a). As the shock passes through the HE, it burns, releasing energy and leaving gaseous detonation products behind. When the shock reaches the HE-metal interface, part of the shock is transmitted into the metal, and part is reflected back into the detonation products. Once the shock reaches the free boundary of the metal jacket, the jacket begins to expand, and part of the shock is again reflected (Figure 2b). As these waves traverse through the system, their interactions with interfaces and boundaries yield additional shocks and rarefaction waves, resulting in complex shock structures as shown in Figure 2c.

A simple two-dimensional schematic of a rate stick experiment and the pressure field at the time of a PDV measurement of interest is shown in Figure 1. To simulate these experiments accurately, many different types of physics must be appropriately accounted for. In addition to hydrodynamics, the HE burn, material strength, melt, and damage behavior must be accurately modeled to cover the wide ranges of material responses that may occur in such an experiment. Developed at Los Alamos National Laboratory, the free Lagrangian hydrodynamics code (FLAG) was used to simulate rate stick experiments (Crowley 2005, Burton 2007).

Simulations in FLAG were run for $K = 14$ different jacket materials, listed in Table 1. All liners use the Mie-Grüniesen solid equation of state (EoS) (Fredenburg et al. 2015), the Steinberg-Cochran-Guinan strength model (Steinberg et al. 1980), a modified analytic Lindemann melt model (Lawson 2009), and a P_{\min} spall

Table 1: Jacket liner materials for the rate stick simulations.

Material	Short Name	Density (g/cc)	Work Hardening
Aluminum 6061	al6061	2.703	125
Aluminum 7075	al7075	2.804	965
Copper	copper	8.930	36
Gold	gold	19.300	49
Gold – 5% Copper	gold_5cu	18.100	1000
Nickel	nickel	8.900	46
Stainless Steel 304	ss304	7.900	43
Stainless Steel 250	ss250	8.129	2
Stainless Steel 4340	ss4340	7.810	2
Tin	tin	7.287	2000
Tungsten	tungsten	19.300	24
Uranium	uranium	19.050	2000
Uranium – 5% Molybdenum	uranium_5mo	18.170	250
Uranium – 0.75% Titanium	uranium_075ti	18.620	1000

damage model (Davison & Stevens 1972). Nominal parameters for each of the metals were obtained from Steinberg et al. (1980).

The FLAG simulation settings for each jacket material constitutes a different physical system with computer model $f_k(\mathbf{x})$, $k = 1, \dots, 14$. We let \mathbf{x} denote the parameters of the Jones-Wilkins-Lee (JWL) EoS (Lee et al. 1968) for PBX 9501, which are shared inputs for all computers. The JWL EoS is given by

$$P(V, e) = A \left(1 - \frac{\omega}{R_1 V}\right) e^{-R_1 V} + B \left(1 - \frac{\omega}{R_2 V}\right) e^{-R_2 V} + \frac{\omega \rho_0 e}{V}, \quad (1)$$

where ρ_0 , A , B , R_1 , R_2 , and ω are physical parameters. This EoS is a function of the normalized specific volume $V = \rho_0/\rho$ and the specific internal energy e . Table 2 gives a range for each input (constructed as nominal value $\pm 3\%$) and the probability distribution for \mathbf{x} is taken to be uniform over the hyper-rectangle defined by these bounds. For each of the 14 jacket materials, 500 simulations are performed using a maximin

Table 2: Nominal JWL parameters for PBX 9501 and their uncertainty ranges.

Input	Parameter	Nominal Value	Lower Bound	Upper Bound
x_1	ρ_0	1.840	1.785	1.895
x_2	A	8.524	8.268	8.780
x_3	B	0.182	0.177	0.187
x_4	R_1	4.550	4.414	4.686
x_5	R_2	1.300	1.261	1.339
x_6	ω	0.380	0.369	0.391

Latin hypercube over the hyper-rectangle defined in Table 2 (Park 1994, Carnell & Carnell 2016). In all cases, other HE characteristics such as the detonation velocities are modified to be consistent with the JWL parameterization (Weseloh 2014).

The primary goal is to find subsets of jacket materials which can be viewed as “neighbors”, in the sense that the computer model for neighboring systems behaves similarly when subjected to perturbations in the input space for \mathbf{x} . In other words, the aim is to find a class (or classes) of computer models for which the gradient is responsive in the same direction of the input space. A secondary goal is to understand the sensitivity of each physical system to the inputs \mathbf{x} and to identify differences in sensitivity across systems.

2.3 Review of Active Subspaces

In the active subspace methodology (ASM) of Constantine (2015), the primary goal is to find a projection of the inputs, i.e., $\mathbf{A}^\top \mathbf{x}$ with $\mathbf{A} = [\mathbf{a}_1 \cdots \mathbf{a}_r]$ and $r \leq p$, such that the output of f is most sensitive to the projected inputs (active variables) $\mathbf{a}_i^\top \mathbf{x}$ ($i = 1, \dots, r$). In particular, the first active direction $\mathbf{a}_1 \in \mathbb{R}^{p \times 1}$ gives the direction which maximizes the expected magnitude of the directional derivative of f with respect to the input distribution μ . Subsequent active directions also maximize this quantity subject to the constraint that they are orthogonal to each of the previous active directions. This is accomplished by first finding the expected outer product of the gradient of f ,

$$C_f = \mathbb{E} [\nabla f(\mathbf{x}) \nabla f(\mathbf{x})^\top] = \int \nabla f(\mathbf{x}) \nabla f(\mathbf{x})^\top d\mu. \quad (2)$$

The matrix C_f provides a wealth of valuable information, and its eigenvalue decomposition $C_f = \mathbf{W} \mathbf{\Lambda} \mathbf{W}^\top$ can be revealing. For some threshold $\tau > 0$, let r be the number of eigenvalues ($\lambda_i = \mathbf{\Lambda}_{ii}$) which are at least τ and let $\mathbf{A} \in \mathbb{R}^{p \times r}$ be the first r columns of \mathbf{W} . The column space of \mathbf{A} is called the active subspace, the i^{th} column of \mathbf{A} (denoted \mathbf{a}_i) is the i^{th} active direction and the linear transformation $\mathbf{a}_i^\top \mathbf{x}$ is the i^{th} projected input. Global sensitivity metrics for each native input ($i = 1, \dots, p$) can be defined as

$$\alpha_i(q) = \sum_{j=1}^q \lambda_j w_{i,j}^2, \quad (3)$$

where $w_{i,j}$ is the $(ij)^{th}$ entry of \mathbf{W} and $q \leq p$ (Constantine & Diaz 2017). The special case $q = 1$ is of notable importance and is often referred to as the *activity score* for input x_i .

3 Co-Active Subspace Methods

K pairwise adjacent functions, f_1, \dots, f_K , are of interest

$$f_k(\mathbf{x}) : \mathcal{X} \mapsto \mathbb{R}, k = 1, \dots, K, \quad (4)$$

with $\mathcal{X} \subset \mathbb{R}^p$. The input vector \mathbf{x} is equipped with a probability distribution $\mathbf{x} \sim \mu$, and therefore the gradient $\nabla f_k(\mathbf{x})$ is a random p-vector because of its dependence on \mathbf{x} . We assume that each function is deterministic, differentiable, and Lipschitz continuous and we define the expected outer product

$$\mathbf{C}_{k\ell} = \mathbb{E}_\mu [\nabla f_k(\mathbf{x}) \nabla f_\ell(\mathbf{x})^\top] = \int \nabla f_k(\mathbf{x}) \nabla f_\ell(\mathbf{x})^\top d\mu, \quad (5)$$

and the expected inner product as

$$t_{k\ell} = \text{trace}(\mathbf{C}_{k\ell}) = \mathbb{E}_\mu [\nabla f_k(\mathbf{x})^\top \nabla f_\ell(\mathbf{x})]. \quad (6)$$

This generalizes the univariate ASM matrix from Equation (2), in the sense that $\mathbf{C}_{kk} = \mathbf{C}_{f_k}$. For notational brevity, we write $\mathbf{C}_{kk} \triangleq \mathbf{C}_k$ and $t_{kk} \triangleq t_k$. When $f_k \neq f_\ell$, we note that $\mathbf{C}_{k\ell}$ is not generally symmetric. It can be useful to define the symmetrized matrix as

$$\mathbf{V}_{k\ell} = \frac{\mathbf{C}_{k\ell} + \mathbf{C}_{\ell k}}{2} \quad (7)$$

and to note that for any unit vector \mathbf{w} the expected product of derivatives in the direction \mathbf{w} is

$$\mathbf{w}^\top \mathbf{C}_{k\ell} \mathbf{w} = \mathbf{w}^\top \mathbf{C}_{\ell k} \mathbf{w} = \mathbf{w}^\top \mathbf{V}_{k\ell} \mathbf{w}. \quad (8)$$

Symmetrizing is useful because it allows us to study the eigendecomposition of $\mathbf{V}_{k\ell}$, drawing many direct comparisons to traditional active subspace methods. This approach, however, masks which function depends on which variables. In order to qualitatively recover this information, the matrices $\mathbf{V}_{k\ell}$, \mathbf{C}_k , and \mathbf{C}_ℓ must be studied simultaneously. An example of this is given in Section 4.1 and Figure 7a and Figure 7b, where the ‘‘co-activity’’ of an input with respect to two functions should be viewed relative to the ‘‘activity’’ of the input for each function individually.

Finally, we note that Lee (2019) recommends a modification to the traditional active subspace, showing that it can improve the discovered subspace when the underlying function is quadratic. Although we do not explore this fully here, this modification can also be applied to the co-active subspace method by replacing $C_{k\ell}$ with

$$\tilde{C}_{k\ell} = \mathbb{E}_\mu [\nabla f_k(\mathbf{x}) \nabla f_\ell(\mathbf{x})^\top] + \mathbb{E}_\mu [\nabla f_k(\mathbf{x})] \mathbb{E}_\mu [\nabla f_\ell(\mathbf{x})]^\top. \quad (9)$$

3.1 Similarity Under Perturbation: Concordance and Discordance

If two functions respond similarly to directional perturbations in the input space, then they are close to each other in some abstract, but important sense. Studying changes in the output of the functions is useful (and should be done), but it is not sufficient by itself to capture all meaningful similarities and fully distinguish between all discrepancies. For instance, the measure $\int |f_1(\mathbf{x}) - f_2(\mathbf{x})|^2 d\mu$ can fail to recognize the close relationship between $f_1(\mathbf{x})$ and $f_2(\mathbf{x}) = a + bf_1(\mathbf{x})$. Looking at the gradients of f_k can provide useful information, so the analysis often benefits from supplementing with measures based on active directions. The Grassmann distance (Ye & Lim 2016) is a useful tool for finding the distance between subspaces, but this approach by itself can fail to solve the problem of interest in some very simple settings. As an extreme example, the Grassman distance is exactly zero when $f_2(\mathbf{x}) = -f_1(\mathbf{x})$. It can also understate how poorly two functions track at the same \mathbf{x} when $f_2(\mathbf{x}) = f_1(\mathbf{x} + \epsilon)$ for fixed $\epsilon \in \mathbb{R}^p$. For example, the functions $f_1(\mathbf{x}) = \sin(c\mathbf{x}^\top \mathbf{1})$ and $f_2(\mathbf{x}) = \sin(c(\mathbf{x} + \epsilon)^\top \mathbf{1})$ will have the similar active subspaces for large values of c and thus the Grassman distance will be small. Yet, the behavior of these functions under perturbation can differ considerably at different locations in the input space. Instead, we propose that, when comparing two non-constant functions, the analysis should be supplemented by a single number, referred to as the *concordance* of f_k and f_ℓ ,

$$\kappa_{k\ell} = \text{conc}(f_k, f_\ell) = \frac{t_{k\ell}}{\sqrt{t_k t_\ell}}, \quad f_k, f_\ell \not\propto 1. \quad (10)$$

Since by Cauchy-Schwarz, $t_{k\ell}^2 \leq t_k t_\ell$, it invariably holds that $\text{conc}(f_k, f_\ell) \in [-1, 1]$. There is a clear analogy here to Pearson's correlation, as the concordance is 1 if and only if $f_\ell(\mathbf{x}) = a + |b|f_k(\mathbf{x})$ and it is equal to -1 if and only if $f_\ell(\mathbf{x}) = a - |b|f_k(\mathbf{x})$ (where the equalities hold almost everywhere with respect to μ). Likewise, the concordance is exactly 0 when the gradient of f_k is almost everywhere orthogonal to the gradient of f_ℓ . It is often convenient to have a formal distance metric, as we will see in Section 4, so we define *discordance* as

$$\text{discord}(f_k, f_\ell) = \sqrt{\frac{1 - \text{conc}(f_k, f_\ell)}{2}}, \quad (11)$$

which satisfies the necessary properties of a pseudo-metric (see Section 3 of the SM). Note that if concordance is the only metric of interest, computation time can be saved by calculating only the diagonal of the $C_{k\ell}$ matrix.

Concordance is appealing as a highly compact summary of the alignment of the gradient spaces of two functions, and the restriction of concordance to the interval $[-1, 1]$ is convenient for interpretation. However, deciding what value of concordance corresponds to “close alignment” of two models is highly context dependent. For example, in most of our applications of interest (multi-physics simulations), it is usually the case that all adjacent models pairs are relatively concordant so that even a small departure from 1 may be meaningful. Much smaller or even negative values of concordance may be routine in other applications.

3.1.1 Simple polynomial example

Code to reproduce all figures and quantities in this section is provided at https://github.com/knrumsey/concordance/inst/CoASM/simple_poly_concordance.R. For illustration throughout this section, consider the functions

$$\begin{aligned} f_1(\mathbf{x}) &= x_1^2 + x_1x_2 \\ f_2(\mathbf{x}) &= x_1^2 + x_1x_2 + \beta x_2^3, \quad \beta \in \mathbb{R}, \end{aligned} \tag{12}$$

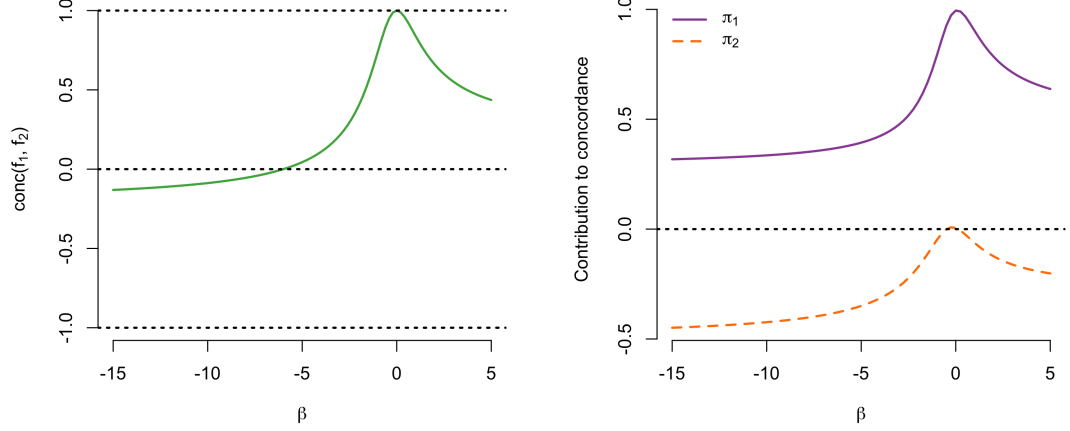
and assume that $x_1, x_2 \stackrel{\text{iid}}{\sim} \text{Unif}(0, 1)$. Here, we have

$$\begin{aligned} \mathbf{C}_1 &= \frac{1}{180} \begin{bmatrix} 480 & 165 \\ 165 & 60 \end{bmatrix}, & \mathbf{C}_2 &= \frac{1}{180} \begin{bmatrix} 480 & 165 + 315\beta \\ 165 + 315\beta & 60 + \beta(324\beta + 180) \end{bmatrix}, \\ \mathbf{C}_{12} &= \frac{1}{180} \begin{bmatrix} 480 & 165 + 315\beta \\ 165 & 60 + 90\beta \end{bmatrix}, & \mathbf{V}_{12} &= \frac{1}{180} \begin{bmatrix} 480 & 165 + \frac{315}{2}\beta \\ 165 + \frac{315}{2}\beta & 60 + 90\beta \end{bmatrix}. \end{aligned} \tag{13}$$

Note that when $\beta = 0$, we have $f_1 = f_2$ and all matrices in Equation (13) become identical. Now, we write

$$\begin{aligned} t_1 &= 3, & t_2 &= 3 + \beta \left(\frac{9}{5}\beta + 1 \right) & t_{12} &= 3 + \frac{1}{2}\beta, \\ \text{conc}(f_1, f_2) &= \frac{3 + \frac{\beta}{2}}{\sqrt{9 + 3\beta \left(\frac{9}{5}\beta + 1 \right)}}. \end{aligned} \tag{14}$$

Figure 3



(a) Concordance between f_1 and f_2 in the simple polynomial example, as a function of β .

(b) The concordance is the sum of the contributions of the first and second co-active directions, $\pi_1 + \pi_2$.

The concordance of f_1 and f_2 , as a function of β , is shown in Figure 3a. When β is relatively small (e.g., $\beta = 1/2$) the functions are intuitively very similar and the concordance is high. As β gets large in magnitude however, the functions become much less concordant. For example, when $\beta = 1/2$ the concordance is 0.944, but the concordance is just 0.551 for $\beta = 3$ and -0.131 for $\beta = -12$.

3.2 Co-Active Directions

As with traditional ASMs, there is much to learn from the eigenvalue decomposition of the expected outer product. To take advantage of the useful properties of the eigendecomposition on symmetric matrices, we focus on the symmetrized matrix $\mathbf{V}_{k\ell}$ rather than $\mathbf{C}_{k\ell}$. Note that, unlike in the one-function case, $\mathbf{V}_{k\ell}$ is potentially indefinite and thus $\mathbf{V}_{k\ell}$ could have negative eigenvalues. We define

$$\mathbf{V}_{k\ell} = \mathbf{W}_{k\ell} \mathbf{\Lambda}_{k\ell} \mathbf{W}_{k\ell}^T, \quad (15)$$

where $\mathbf{W}_{k\ell}$ is a $p \times p$ orthonormal matrix of eigenvectors $\mathbf{w}_i^{(k\ell)}$ ($i = 1, \dots, p$) and $\mathbf{\Lambda}_{k\ell}$ is a diagonal matrix of eigenvalues $\lambda_i^{(k\ell)} = (\mathbf{\Lambda}_{k\ell})_{ii}$ ordered from largest ($\lambda_1^{(k\ell)}$) to smallest ($\lambda_p^{(k\ell)}$).

We refer to the leading columns of $\mathbf{W}_{k\ell}$ as the *co-active directions*, noting that (by Equation (8) and properties of an eigendecomposition) the first such direction, $\mathbf{w}_1^{(k\ell)}$, maximizes the expected product of directional

derivatives, and the subsequent directions maximize the same quantity while maintaining orthogonality between all previous co-active directions. That is,

$$\begin{aligned} \mathbf{w}_1^{(k\ell)} &= \arg \max_{\mathbf{w}: \|\mathbf{w}\|=1} \int (\mathbf{w}^\top \nabla f_k(\mathbf{x})) (\mathbf{w}^\top \nabla f_\ell(\mathbf{x})) d\mu \\ \mathbf{w}_j^{(k\ell)} &= \arg \max_{\substack{\mathbf{w}: \|\mathbf{w}\|=1 \\ \mathbf{w}^\top \mathbf{w}_i^{(k\ell)}=0, (i < j)}} \int (\mathbf{w}^\top \nabla f_k(\mathbf{x})) (\mathbf{w}^\top \nabla f_\ell(\mathbf{x})) d\mu, \quad j = 2, \dots, p. \end{aligned} \quad (16)$$

Moreover, the eigenvalues satisfy

$$\lambda_i^{(k\ell)} = \mathbf{w}_i^{(k\ell)\top} \mathbf{V}_{k\ell} \mathbf{w}_i^{(k\ell)} = \int (\mathbf{w}_i^\top \nabla f_k(\mathbf{x})) (\mathbf{w}_i^\top \nabla f_\ell(\mathbf{x})) d\mu, \quad (17)$$

which indicates that λ_i is large (in magnitude) if the expected value of the product of directional derivatives is large (in magnitude). That is, the i^{th} eigenvalue is large only if both functions are active in the direction of the i^{th} eigenvector in some region of the input space. Positive eigenvalues indicate that upon perturbation in the direction of $\mathbf{w}_i^{(k\ell)}$, both functions change in the same way (i.e., both increase, or both decrease) and negative values imply the opposite (i.e., one function increases while the other decreases). We can tie this back to concordance by noting that, since $t_{k\ell} = \text{tr}(\mathbf{V}_{k\ell}) = \text{tr}(\mathbf{\Lambda}_{k\ell})$ (and because $t_k, t_\ell \geq 0$), the concordance of f_k and f_ℓ can be negative (or positive) only when the sum of the eigenvalues is negative (or positive). Eigenvalues which are small in magnitude can occur in one of two ways. Most commonly, this occurs because (at least) one of the two functions f_k or f_ℓ is constant or nearly constant in the direction of the corresponding eigenvector, for every point in the input space. This can also occur if the effect of moving along the active direction has opposite effect on the response for various regions of the input space.

To aid in the interpretation of the eigenvalues, it is sometimes helpful to view them in their standardized form

$$\pi_i^{(k\ell)} = \frac{\lambda_i^{(k\ell)}}{\sqrt{t_k t_\ell}}. \quad (18)$$

We call these quantities *contributions* because they indicate the degree to which variation along each co-active direction contributed to the concordance. In particular, note that $\sum_{i=1}^p \pi_i^{(k\ell)} = \text{conc}(f_k, f_\ell)$. In the case where $f_k = f_\ell$, the contributions are certain to be positive and so $\pi_i^{(k)}$ reduces to the proportion of the total gradient. In the case where $f_k \neq f_\ell$, the contributions cannot be interpreted as proportions, but their signs and magnitudes still carry valuable and interpretable information about the co-active directions.

3.2.1 Low Dimensional Representation of Adjacent Models

Much of the literature for ASM motivates active directions through a Gaussian Poincaré inequality that bounds the mean squared error (MSE) in approximating a target function by its conditional expectation on a linear subspace of the inputs. Active directions minimize the Poincaré bound. For example, if $\mu = \mathcal{N}_p(\mathbf{m}, \Sigma)$ then Proposition 2.5 of Zahm et al. (2020) bounds the approximation MSE on the r dimensional subspace $\mathcal{B} = \text{span}(\mathbf{B}) \subset \mathbb{R}^p$ where the r columns of \mathbf{B} are linearly independent input directions:

$$\int (f(\mathbf{x}) - \hat{f}(\mathbf{x}))^2 d\mu \leq \text{trace}(\Sigma(\mathbf{I} - \mathbf{P}_B)\mathbf{C}_f(\mathbf{I} - \mathbf{P}_B)), \quad (19)$$

where \mathbf{C}_f was defined in Equation (2), $\mathbf{P}_B = \mathbf{B}(\mathbf{B}^\top \mathbf{B})^{-1} \mathbf{B}^\top$ is the projection matrix onto \mathcal{B} , and $\hat{f}(\mathbf{x}) = \mathbb{E}_{\mathbf{X} \sim \mu}[f(\mathbf{X}) | \mathbf{P}_B \mathbf{X} = \mathbf{P}_B \mathbf{x}]$ is the conditional expectation on \mathcal{B} . Transforming to canonical coordinates $\tilde{\mathbf{x}} = \Sigma^{-1/2} \mathbf{x}$ and setting \mathbf{B} to be the first r resulting AS directions minimizes the bound for a linear subspace of dimension r (Zahm et al. 2020, Proposition 2.6, simplified). On the other hand, setting \mathbf{B} to the leading columns of $\mathbf{W}_{k\ell}$ (i.e. Equation (15)) produces approximation bounds for $f = f_k$ and $f = f_\ell$ on the co-active subspace and, in general, these bounds will be larger than the optimal AS bounds for the same subspace dimension.

But co-active directions have a different goal; they capture the subspace on which the gradients of two functions are best aligned. In a high concordance situation, the co-active subspace will also be suitable for approximating the two functions, but this is not the primary purpose. Along these lines, Section 4.2 compares approximation errors on a variety of different subspaces in the high explosive application.

To determine an appropriate size of the lower dimensional subspace, one can adopt the common approach for single-function active subspaces, which is to look for gaps in the eigenvalues. This can be done visually or via a sequential testing procedure (Ma & Zhu 2013). The only distinction for co-ASM is the possibility of negative eigenvalues, and so they should be ordered by their absolute magnitude rather than the conventional ordering.

3.2.2 Simple polynomial example

In the high-concordance case of $\beta = 1/2$, the first active directions for f_1 and f_2 are, respectively, $\mathbf{w}_1^{(1)} \approx [0.945 \ 0.327]^\top$ and $\mathbf{w}_1^{(2)} \approx [0.825 \ 0.566]^\top$. These active directions are similar, but it does correctly indicate that x_2 is relatively more important for f_2 than for f_1 . The first co-active direction is given by $\mathbf{w}_1^{(12)} \approx [0.907 \ 0.422]^\top$, the optimal compromise between the active directions. The contribution vector is $\boldsymbol{\pi}^{(12)} =$

[0.9518 − 0.0077]. From these quantities, we learn that moving in the direction $0.907x_1 + 0.422x_2$ leads to substantial changes on average in magnitude for both f_1 and f_2 (in the same direction). Moving orthogonal to this direction leads to less substantial, but non-zero, changes in the output of f_1 and f_2 in opposite directions. The contributions, $\pi_1^{(12)}$ and $\pi_2^{(12)}$, are plotted in Figure 3b as a function of β .

3.3 Co-sensitivity Analysis

We now turn our attention to assessing the sensitivity of the functions to the native inputs. By straightforward extension of the activity score sensitivity metric given in Equation (3), we define the *signed co-activity score* for input x_i with respect to f_k and f_ℓ to be

$$\alpha_i^{(k\ell)}(q) = \sum_{j=1}^q \lambda_{i_j}^{(k\ell)} \left(w_{i,i_j}^{(k\ell)} \right)^2, \quad (20)$$

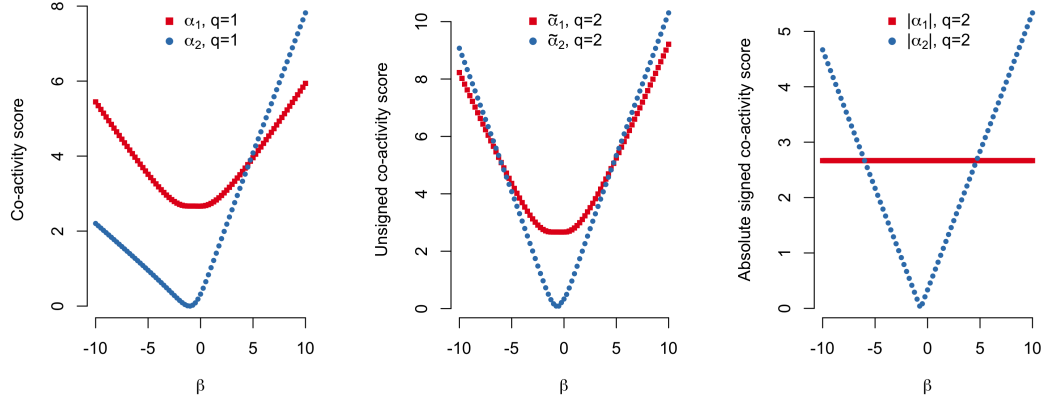
where the indices i_1, \dots, i_p represent a permutation of the set $\{1, \dots, p\}$ such that

$$\left| \lambda_{i_1}^{(k\ell)} \right| \geq \left| \lambda_{i_2}^{(k\ell)} \right| \geq \dots \geq \left| \lambda_{i_p}^{(k\ell)} \right|.$$

This extra step is necessary since the magnitude of the eigenvalues signals the importance of an active direction, regardless of sign. Following the advice of Constantine & Diaz (2017) we recommend setting $q = 1$, but it is also sometimes reasonable to set $q = r$ where r is the number of eigenvalues which exceed some threshold $\tau > 0$ in absolute value. The signed co-activity score can be positive or negative, and this single bit of information carries useful information about the relationship of the corresponding input to the functions f_k and f_ℓ . When the i^{th} co-activity score is negative, the net effect of input x_i is positive for one of the functions and negative for the other. When $q > 1$, it is possible for the terms in Equation (20) to cancel out, masking the importance of a particular variable. To account for this, we introduce the *unsigned co-activity score* for input x_i with respect to f_k and f_ℓ to be

$$\tilde{\alpha}_i^{(k\ell)} = \sum_{j=1}^q \left| \lambda_{i_j}^{(k\ell)} \right| \left(w_{i,i_j}^{(k\ell)} \right)^2. \quad (21)$$

This sensitivity index can be interpreted like the traditional activity score, in the sense that large positive values indicate that a variable is highly active in functions f_k and f_ℓ , although the “direction” of the activity is lost. When $q = 1$, the signed and unsigned co-activity scores can differ only in their sign, e.g., $\alpha_i^{(k\ell)} = \pm \tilde{\alpha}_i^{(k\ell)}$ – a fact that fails to hold true for $q > 1$.



(a) Co-activity scores for the native inputs x_1 and x_2 as a function of β . When $q = 1$, the signed and unsigned scores are equivalent (up to sign).
 (b) Unsigned co-activity scores (with $q = 2$) for the native inputs x_1 and x_2 as a function of β .
 (c) Absolute value of the signed co-activity scores (with $q = 2$) for the native inputs x_1 and x_2 as a function of β .

Figure 4

3.3.1 Simple polynomial example

Some co-activity scores are shown for the simple polynomial example in Figure 4. When $q = 1$, the absolute-signed and unsigned co-activity scores are equivalent, and they demonstrate that x_1 is jointly more important to the functions for $\beta \lesssim 5$ and x_2 is relatively more active otherwise. In the $q = 2$ case, the unsigned activity scores are plotted in Section 3.3 and the absolute value of the signed activity scores are plotted in Section 3.3. According to both of these metrics, x_2 becomes more co-active for f_1 and f_2 when $|\beta| \gtrsim 5$.

3.4 Efficient Numerical Approximation

So far, we have been working with an extremely simple example which has allowed for closed form analysis of the co-active subspace, but most interesting and important problems will not be so tractable. Thus, numerical tools are needed to perform these analyses accurately and efficiently. In particular, we need a way to estimate the matrix $C_{k\ell}$ when it is not available analytically, as is usually the case. This is the same computational and theoretical bottleneck faced in traditional active subspace methodology, where the majority of the literature has relied on Monte Carlo (MC) estimation (Constantine & Gleich 2014, Constantine 2015). In

the MC approach, we assume that the gradient of each f_k ,

$$\nabla f_k(\mathbf{x}) : \mathbb{R}^p \mapsto \mathbb{R}^p,$$

can be calculated (or estimated) quickly and accurately. Then, we simply iterate between (i) sampling $\mathbf{x}_b \sim \mu$ and (ii) calculating $\hat{\mathbf{C}}_b^{(k\ell)} = \nabla f_k(\mathbf{x}_b) \nabla f_\ell(\mathbf{x}_b)^\top$ for $b = 1, \dots, B$; the final estimator can now be constructed as

$$\hat{\mathbf{C}}_{k\ell} = \frac{1}{B} \sum_{b=1}^B \hat{\mathbf{C}}_b^{(k\ell)}. \quad (22)$$

Although this approach is appealing for its simplicity, it is associated with many notable drawbacks. For high-dimensional functions (e.g., large p) the method can be slow to converge and does not easily lend itself to uncertainty estimation. Further, it requires computer experiments to be tailored specifically to the probability distribution μ , which disallows the use of previously existing data sets and does not permit meta-analysis over multiple distributions (as in robust Bayes; Berger (1990)). Importance weighting could be incorporated into the procedure for this purpose, but this is seldom an efficient use of computer resources.

A recent alternative (Wycoff et al. 2021, Rumsey, Francom & Vander Wiel 2023), is based on fitting an emulator (or surrogate-model) to data in order to learn the input-output map defined by each f_k . Conditional on this statistical emulator, the $\mathbf{C}_{k\ell}$ matrix can be efficiently and accurately computed. In this paper, we generalize the approach discussed by Rumsey, Francom & Vander Wiel (2023), which has been shown to perform well in high-dimensional (large p) settings. The first step is to represent each function f_k , ($k = 1, \dots, K$) as closely as possible by a model of the form,

$$f_k(\mathbf{x}) \approx \gamma_{k0} + \sum_{m=1}^{M_k} \gamma_{km} \prod_{i=1}^p [s_{kim}(x_i - t_{kim})]_+^{u_{kim}}, \quad (23)$$

where $[x]_+ = \max(x, 0)$ is called a hinge function, $s_{kim} \in \{-1, 1\}$ is a sign, t_{kim} is a knot and $u_{kim} \in \{0, 1\}$ is a variable inclusion indicator. This linear combination of multivariate splines is known to have the universal representation property (Lin & Unbehauen 1992). A popular algorithm for fitting models of the form in Equation (23) is known as multivariate adaptive regression splines (MARS) (Friedman 1991, Denison et al. 1998). The Bayesian additive spline surfaces (BASS) algorithm of Francom & Sansó (2020) represents a modernized version of the algorithm (with parallel tempering, g -priors, flexible likelihoods, and cleverly constructed proposal distributions) which has been successfully applied to a wide range of UQ problems (Francom et al. 2018, 2019, Rumsey et al. 2024, Nott et al. 2005) and has proven to be a highly competitive

emulator in recent comparisons (Collins et al. 2024, Hutchings et al. 2023, Rumsey, Huerta & Derek Tucker 2023). For the sake of brevity, we leave additional details to the references, especially Francom et al. (2018) and Francom & Sansó (2020).

We note that a similar approach can be developed for alternative emulators (including Gaussian processes and additive regression trees), but BASS has been shown to be effective and efficient; see Rumsey, Francom & Vander Wiel (2023) for a detailed discussion and comparison of alternatives for a single-function active subspace.

Given two functions f_k and f_ℓ , we can write the $(i,j)^{th}$ element of $C_{k\ell}$ as

$$C_{k\ell}[i, j] = \int \frac{\partial f_k}{\partial x_i}(\mathbf{x}) \frac{\partial f_\ell}{\partial x_j}(\mathbf{x}) \mu(\mathbf{x}) d\mathbf{x} \quad (24)$$

This high-dimensional integral will be intractable for most problems of interest, but by representing each function in the form of Equation (23), we can generalize the calculations of Rumsey, Francom & Vander Wiel (2023) and write

$$C_{k\ell}[i, j] = \begin{cases} \sum_{m_1=1}^{M_k} \sum_{m_2=1}^{M_\ell} \gamma_{km_1} \gamma_{\ell m_2} I_{3,k\ell}^{(i)}[m_1, m_2] \prod_{i' \neq i} I_{2,k\ell}^{(i')}[m_1, m_2], & i = j \\ \sum_{m_1=1}^{M_k} \sum_{m_2=1}^{M_\ell} \gamma_{km_1} \gamma_{\ell m_2} I_{1,k\ell}^{(i)}[m_1, m_2] I_{1,\ell k}^{(j)}[m_2, m_1] \prod_{i' \notin \{i, j\}} I_{2,k\ell}^{(i')}[m_1, m_2], & i \neq j, \end{cases} \quad (25)$$

Where $I_{1,k\ell}^{(i)}[m_1, m_2]$, $I_{2,k\ell}^{(i)}[m_1, m_2]$, and $I_{3,k\ell}^{(i)}[m_1, m_2]$ are univariate integrals which can be solved in closed form, so long as $\mu(\mathbf{x}) = \prod_{i=1}^p \mu_i(x_i)$, corresponding to statistical independence of the x_i . To construct $C_{k\ell}$ in its entirety, we need to evaluate $4pM_kM_\ell$ such integrals, but the closed form availability of the solution makes the algorithm incredibly fast in practice. Additional details, including the tractable solution to $I_{c,k\ell}^{(i)}[m_1, m_2]$, $c = 1, 2, 3$, are given in Section SM3.

Software to estimate $C_{k\ell}$ accurately and efficiently using the method described above is provided in the R package `concordance` which can be found at <https://github.com/knrumsey/concordance>. Using similar methods to the above, the software can also approximate the modification proposed by Lee (2019), given in Equation (9) (see SM3 for details). A numerical study of the Piston function (Zacks 1998) is provided in Section SM4 in order to demonstrate the accuracy of the proposed approach for a moderately high-dimensional model.

3.4.1 Simple polynomial example

We will demonstrate the speed and accuracy of the described approach by using it for the simple polynomial example of Equation (12) with $\beta = 3$. We begin by sampling $n = 200$ input locations using a maximin Latin hypercube, $\{\mathbf{x}_1, \mathbf{x}_2, \dots, \mathbf{x}_n\}$ (Park 1994). For each of the generated inputs, we evaluate f_1 and f_2 , and use the `BASS` R package to learn a representation of these functions in the form of Equation (23). This takes 6.9s and 7.2s for f_1 and f_2 respectively, using a 2019 MacBook Pro with a 2.8 GHz Quad-Core Intel Core i7. Using these representations, we use Equation (25) to estimate C_1 , C_2 and C_{12} . Using the `c_bass` and `cfg_bass` functions from the `concordance` package, an estimate was obtained for all 3 matrices in just 0.233 seconds. The estimated and true C_{12} matrices are

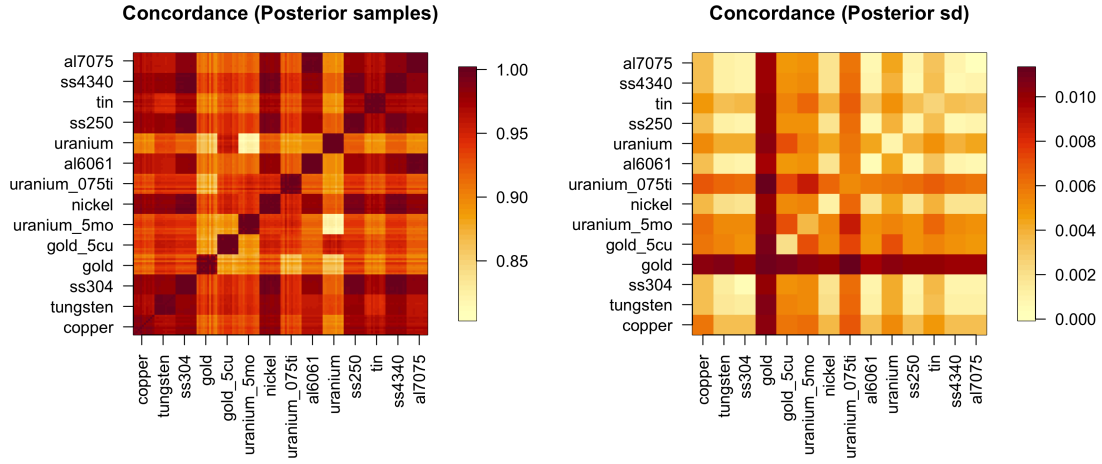
$$C_{12}^{\text{true}} \approx \begin{bmatrix} 2.667 & 6.167 \\ 0.917 & 1.833 \end{bmatrix}, \quad C_{12}^{\text{est}} = \begin{bmatrix} 2.634 & 6.086 \\ 0.896 & 1.790 \end{bmatrix}, \quad (26)$$

with a Frobenius distance (Golub & Van Loan 2013) between the two matrices of 0.050. If we increase the size of the training set to $n = 1000$, the `BASS` models take between 21 and 32 seconds to fit, the matrices can be estimated with the `concordance` package in 1.14 seconds, and the Frobenius distance decreases to 0.0086. For a detailed scaling study and for details on the choice of prior $\mu(\mathbf{x})$, see Rumsey, Francom & Vander Wiel (2023).

4 Application to High Explosives

We now return to the computer experiments for PBX 9501 described in Section 2.2. The co-active subspace methods developed in Section 3 will be deployed in order to answer scientific questions of interest. The data and the R code used to generate many of the figures and quantities in this section can be found at <http://github.com/knrumsey/PBX9501>.

For each of the $K = 14$ functions (corresponding to different jacket materials), the 500 computer model runs are used to train a Bayesian MARS model, using the `BASS` package (Francom & Sansó 2020), so that each f_k can be represented in the form of Equation (23). In each case, the `BASS` model required about 10 seconds to learn the appropriate representation. The 14 model fits were validated using 100-fold cross validation (CV) (Stone 1978), where the CV root mean square prediction error (RMSPE) was found to be between 0.006 and 0.108 (the response was scaled to have unit variance). The worst model fits were obtained for gold, uranium and gold + 5% copper.



(a) The estimated concordance for each of the 9370 model pairs. The blocks represent posterior samples of the concordance estimate for pairs of jacket materials.

(b) The posterior standard deviation for the pairwise concordance estimates. Even in the worst case, the posterior standard deviation is quite small.

Figure 5

The posterior distribution of a BASS model can be viewed as an ensemble of MARS models. To account for uncertainty in the fits, we obtain 10,000 ensemble members discarding the first 9,000 for burn-in and thinning down to 10 posterior samples (e.g., ensemble members) for each of the 14 cases leading to a total of 140 different functions of interest. The choice of ten ensemble members per computer model is arbitrary, and should be chosen according to the computational budget. In total, there are $\binom{14 \times 10}{2} = 9730$ $C_{k\ell}$ matrices that must be estimated (on top of the 140 C_k matrices); a monumental task for MC based estimation. Fortunately, using the techniques developed in Section 3.4, the `concordance` package is able to conduct the entire analysis in under half an hour on a 2019 MacBook Pro. For all 9730 cases, the concordance is computed for the function pair using Equation (10).

Each computer model, corresponding to a particular jacket material, is represented in the analysis by 10 functions. Thus for each pair of computer models (two distinct metals), there are 100 function combinations and thus 100 “posterior draws” for the concordance. These samples can be seen in Figure 5a, where the underlying 14×14 structure can easily be seen in the checkerboard pattern of each block. The overall estimate (posterior mean) of concordance for two metals (e.g., gold and copper), is obtained by averaging the values in the corresponding block. The posterior standard deviation, as seen in Figure 5b, is calculated similarly. The relatively small posterior standard deviations indicate precise estimates, with the most uncertainty occurring

when computing the concordances for gold. Explicit values for the posterior means and standard deviations are reported in Section SM5.

At present, it is challenging (or at least time-consuming) to gain insight into things by simply staring at Figure 5. Some interesting observations are apparent; all concordance values are positive and reasonably large, yet we notice the relatively low concordance (0.820) between the computer models with a uranium jacket and a uranium - 5% Molybdenum jacket, which is surprising. General conclusions are hard to come by. To better illustrate these findings, we propose the following procedure: (i) convert the 140×140 concordance matrix into a “discordance matrix” by applying Equation (11) elementwise, (ii) use a multidimensional scaling (MDS) method (we choose Kruskal’s non-metric MDS here; Kruskal (1964), Mead (1992)) to project the 140 functions into a 2D space such that the Euclidean distance between points is approximately proportional to the discordance and (iii) define a point “center” (e.g., first moment of the posterior point cloud) for each of the 14 computer models and partition the 2D space using a Voronoi diagram (Okabe et al. 2009).

By following this approach, as seen in Figure 6, the similarities and differences in the gradients of the various models become clearer and neighborhoods become easier to define and more intuitive to interpret. Each

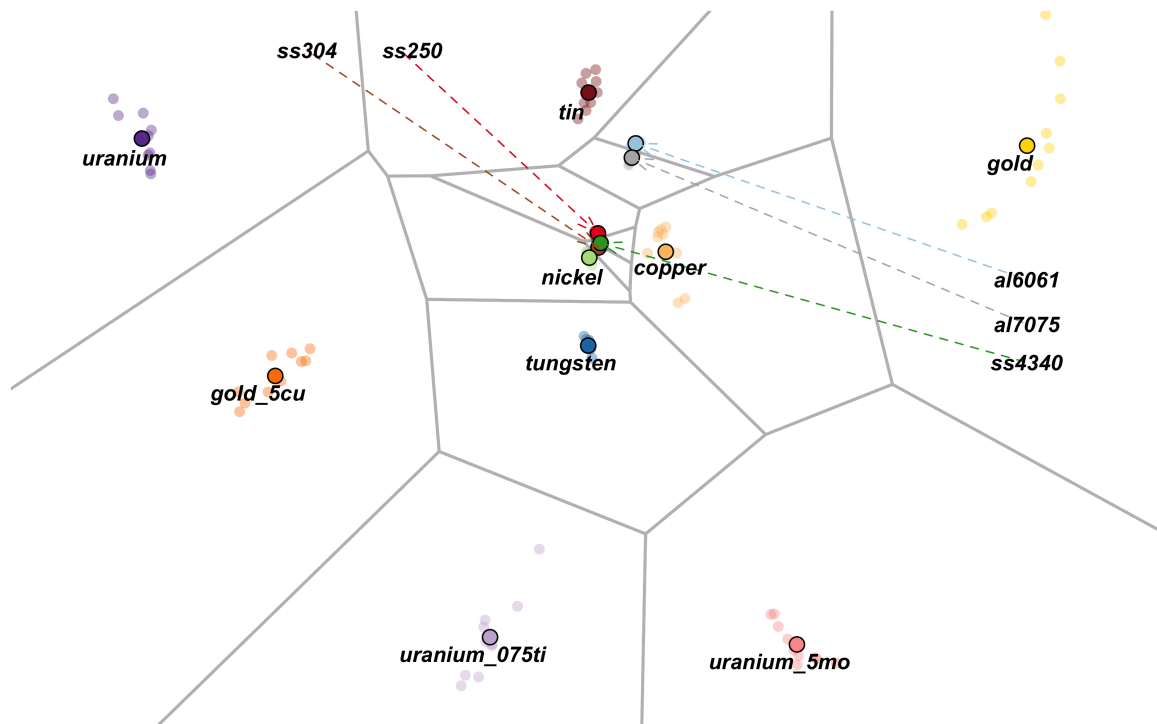


Figure 6: Clustering of jacket materials based on multidimensional scaling of discordance.

metal jacket is defined by a large number of system variables that define the EoS, strength, melt, and damage models. Although one can reasonably assume that some system variables, such as material density, strongly influence the velocity of the jacket at the PDV measurement location and time, the exact relationship between these variables and the resulting output is unknown, and likely quite complex. With this, it can be expected that a concordance analysis will bolster these underlying assumptions, and perhaps yield additional insights into the relationship between the system variables and PDV outputs. At the outset, it was assumed that density was the most determinate factor in the resultant PDV measurement. The denser the jacket, the slower it will move. Moderate density materials such as nickel, stainless steel, tin, and copper were expected to be more concordant with one another than with low densities, like aluminum, or high density materials, like uranium, tungsten, or gold. Upon initial investigation, Figure 6 seems to bear this out, however, there are some notable discrepancies within the high density materials. Namely, gold is more concordant with lower density materials than its high density counterparts. As it turns out, gold is a quite soft metal compared to others in the set, such as uranium. The hardness of a metal, measured by the work hardening parameter in Table 1, determines how resistant it is to deformation. A soft metal, therefore, may deform much more than a hard metal, resulting in notably different velocity measurements. Close inspection of Table 1 and Figure 6 provide evidence for this claim. For example, tungsten, the softest of the high density jackets is more concordant with gold than any other. Further, as the hardness of the high density jackets increases, the concordance with gold decreases. It is clear that there is much more influencing the PDV output than merely the density and hardness, however, the concordance analysis not only confirmed the initial hypothesis of a strong correlation to density, but also highlighted an unexpected additional relationship between the system variables and the PDV output. We note that this example and the associated discussion are closely related to Q1 and Q2 in Section 2.1.

4.1 Co-Sensitivities

To continue the analysis, we will take a closer look at the co-active subspace and some related quantities. The questions we seek to answer in this subsection can be seen as an expanded version of Q3 from Section 2.1. For simplicity, we reduce the scope slightly and focus on just 3 jacket materials: Stainless Steel 304 (SS), Nickel (Ni) and Uranium (U). From Figure 6 we can see that SS and Ni are neighbors in the sense that they are highly concordant ($\text{conc}(f_{SS}, f_{Ni}) = 0.996$), suggesting that they behave similarly under directional perturbation and are likely to be sensitive to the inputs in a similar way. Uranium, on the other hand, is much less concordant with the other two materials ($\text{conc}(f_U, f_{Ni}) = 0.921$, $\text{conc}(f_U, f_{SS}) = 0.918$). In all cases, the active and co-active subspaces are effectively one-dimensional. This can be seen by examination

Table 3: The contribution vectors suggest that the majority of the co-activity is found in one direction.

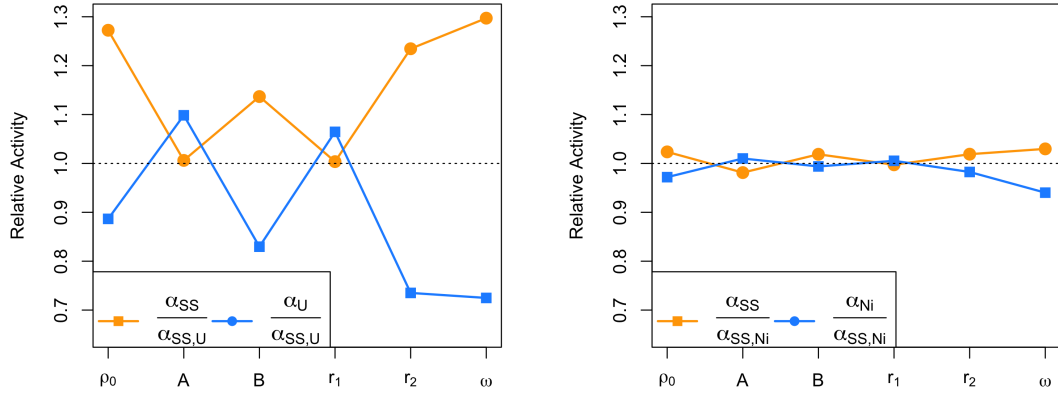
	Co-active direction					
	1	2	3	4	5	6
$\pi^{SS, Ni}$	0.995	0.0004	0.0004	0.0002	0.0001	0.00002
$\pi^{Ni, U}$	0.924	0.001	0.001	0.0001	-0.0003	-0.004
$\pi^{SS, U}$	0.922	0.001	0.0003	0.00002	-0.0002	-0.005

of the contribution vectors, reported in Table 3, which show that the concordance can be almost entirely attributed to the first co-active direction. Since each π_i is positive for the combination of SS and Ni, we learn that all active directions lead to concordant changes in the output of the computer models. The negative contributions π_5 and π_6 for the combination of U and SS (or equivalently U and Ni), indicate that moving along the 5th and 6th active direction has an opposite average-effect on the two functions. Note also that, for both combinations involving U, the 6th contribution vector is the second largest in magnitude, and hence the corresponding active direction is actually the second most influential, though it is effectively negligible compared to the dominant direction.

Table 4: Activity and co-activity scores for Stainless Steel 304 (SS), Nickel (Ni) and Uranium (U). In all cases, the output of the computer model is most sensitive (or co-sensitive) to r_1 and least sensitive (or co-sensitive) to ω .

	Native input					
	ρ_0	A	B	r_1	r_2	ω
$10^3 \times \alpha^{SS}(1)$	5.968	4.447	3.835	20.340	6.922	1.492
$10^3 \times \alpha^{Ni}(1)$	5.666	4.578	3.741	20.506	6.675	1.362
$10^3 \times \alpha^U(1)$	4.158	4.855	2.799	21.575	4.122	0.833
$10^3 \times \alpha^{SS, Ni}(1)$	5.830	4.532	3.764	20.397	6.794	1.448
$10^3 \times \alpha^{Ni, U}(1)$	4.561	4.485	3.312	20.350	5.495	1.125
$10^3 \times \alpha_{SS, U}(1)$	4.690	4.420	3.373	20.266	5.607	1.150

Since the dominant (largest in magnitude) component of the contribution vector is positive, the signed and unsigned co-activity scores will be identical for the choice $q = 1$. The activity and co-activity scores are reported in Table 4. Since all values are positive, we can deduce that the inputs affect the different computer models in the same “direction”. That is, increasing an input x_i leads to an average increase (or decrease) in the output for both functions. The relative differences vary however, indicating that a particular JWL input is more “important” for one function over the other. The ratios $\alpha_i^k/\alpha_i^{k\ell}$ and $\alpha_i^\ell/\alpha^{k\ell}$ ($i = 1, \dots, p$) provide a useful visualization for understanding (i) which function is more sensitive to each input and (ii) the degree of



(a) The relative activity of SS and U to their joint co-activity. We see that SS is much more sensitive to ρ_0 , B, r_2 and ω than U.

(b) The relative activity of SS and Ni to their joint co-activity. We see that SS is more sensitive to ρ_0 , B, r_2 and ω than Ni, but the difference is hardly of practical significance.

Figure 7

difference between the functions. Two examples of this are given in Figure 7a and Figure 7b, where we see that SS is more sensitive to perturbations in ρ_0 , B, r_2 and ω compared to both U and Ni, but the magnitude of the ratios are much more substantial when comparing to uranium.

4.2 Low Dimensional Representation of JWL

Finally, consider the problem of finding a suitable transformation of the JWL parameters for PBX 9501 with reduced dimension (i.e., Q4 in Section 2.1). One of the most valuable features of ASM is its ability to answer this question. The traditional active subspace is, however, tailored to a single function and may not be appropriate for two or more functions. The co-active subspace analysis yields a solution to this problem for the two-function case. To demonstrate, the $p = 6$ dimensional input data is projected down to 2 dimensions using (i) the first and second active directions of f_{SS} , (ii) the first and second active directions of f_U , and (iii) the first and sixth co-active directions of f_U and f_{SS} (recall that $\pi_6^{SS,U}$ has the second largest absolute contribution). Finally, we compare to the approach described in Zahm et al. (2020), which is specifically designed for this purpose and reduces to projecting onto the first two eigenvectors of $\mathbf{H} = \mathbf{C}_{SS} + \mathbf{C}_U$.

Table 5: Cross validation RMSPE values for BASS regression models for the PDV response (scaled to have unit variance), corresponding to Stainless Steel 304 (SS) and Uranium (U). The models were trained using various $2D$ projections of the input data. The projection onto the co-active subspace leads to accurate predictions for both materials simultaneously.

	Full Data	C_{SS}	C_U	$V_{SS,U}$	H
Stainless Steel 304	0.011	0.022	0.145	0.023	0.038
Uranium	0.074	0.117	0.078	0.101	0.097

For each of these projected inputs, we fit non-linear surrogate models using the R BASS package (Francom & Sansó 2020) to predict the PDV velocity (see Figure 1) in the experiments for Stainless Steel 304 and for Uranium. Shown in Table 5, the quality of each fit is assessed by the 50-fold cross validation RMSPE. The projected inputs designed specifically for one material led to good predictions for the intended material; the predictions are substantially less accurate when used to predict outcomes for the other material. The inputs projected onto the co-active subspace, on the other hand, lead to reasonably good predictions for both materials concurrently. Similar behavior is observed when projecting onto the H matrix of Zahm et al. (2020), although the accuracy of the reduced model for Stainless Steel 304 is considerably worse when projecting onto H compared to $V_{SS,U}$. We do acknowledge, however, that Zahm et al. (2020) could be used to construct a shared active subspace for all 14 materials at once, while co-active subspaces (in their current form) are only useful for two functions at a time.

5 Conclusion

In this paper, we have extended the active subspace methodology of (Constantine 2015) in a manner that not only aligns naturally with our problem but also introduces a novel dimension to this powerful tool. Other methods, such as the multivariate extension of Zahm et al. (2020) find shared active directions but are blind to whether the functions respond in a coordinated fashion along those directions. Co-active subspace analysis captures the *sign* of correlated activity and degree of coordination shared by the two functions as they respond to input perturbations.

As described in the introduction, co-activity is one of several approaches being used to demonstrate the functional equivalence of a new design with trusted, established systems. Our argument revolves around the high concordance observed between the new design and several well-established systems. This concordance suggests that the new design reacts similarly to input perturbations, and with further insights into the underlying physics, this congruence can help formulate a compelling case that the same dominant physical phenomena

are at play. It is important to recognize that this work is not exhaustive, and further refinement of this argument is warranted. One avenue we propose is the use of the discordance matrix across a collection of related systems. This approach enables us to quantitatively assess the proximity of each system to the new design and explore the possibility of partitioning the systems into meaningful clusters. The quantitative measure of similarity between the new design and trusted systems plays a pivotal role in bolstering our overall confidence in the new design, particularly when the feasibility of full-system testing is constrained.

Looking ahead, there are promising avenues for extension. The current framework, which focuses on pairwise comparisons, could be further developed to accommodate more than two functions, enabling a more comprehensive analysis. Additionally, temporal or spatial variations could be explored to address the nuances of dynamic systems.

Despite its utility, we have noted the limitations that arise from symmetrizing the C_{fg} matrix. Future work could focus on studying C_{fg} directly, perhaps through its singular value decomposition, in the pursuit of a fully comprehensive analysis. Finally, *active manifolds* (Bridges et al. 2019) extend AS methods to find nonlinear streamline curves through the input space along which the output maximally varies. Conceptually, a co-active manifold would find a curve along which the gradients of two adjacent models are maximally aligned. These extensions hold the potential to expand the applicability of our methodology to a wider array of complex engineering challenges.

Supplemental Materials

The supplemental materials include additional details for the rate stick experiments, a proof that discordance satisfies the properties of a pseudo-metric, implementation details (including a brand new derivation of the expected gradient in closed-form for models in the form of Equation (23)), a higher-dimensional example using the Piston function (Zacks 1998), and posterior means and standard deviations corresponding to Section 4.1. An R package is also available and can be found at <https://github.com/knrumsey/concordance>.

References

Batta, I., Abrol, A. & Calhoun, V. (2021), Uncovering active structural subspaces associated with changes in indicators for alzheimer’s disease, in ‘2021 43rd Annual International Conference of the IEEE Engineering in Medicine & Biology Society (EMBC)’, IEEE, pp. 3948–3951.

- Ben-Ari, E. N. & Steinberg, D. M. (2007), ‘Modeling data from computer experiments: an empirical comparison of kriging with mars and projection pursuit regression’, *Quality Engineering* **19**(4), 327–338.
- Berger, J. O. (1990), ‘Robust bayesian analysis: sensitivity to the prior’, *Journal of statistical planning and inference* **25**(3), 303–328.
- Bernstein, J., Schmidt, K., Rivera, D., Barton, N., Florando, J. & Kupresanin, A. (2019), ‘A comparison of material flow strength models using bayesian cross-validation’, *Computational Materials Science* **169**, 109098.
- Bridges, R., Gruber, A., Felder, C., Verma, M. & Hoff, C. (2019), Active manifolds: A non-linear analogue to active subspaces, in ‘International Conference on Machine Learning’, PMLR, pp. 764–772.
- Buede, D. M. & Miller, W. D. (2016), ‘The engineering design of systems: models and methods’.
- Burton, D. E. (2007), Lagrangian hydrodynamics in the flag code, in ‘Symposium on Advanced Numerical Methods for Lagrangian Hydrodynamics’.
- Carnell, R. & Carnell, M. R. (2016), ‘Package ‘lhs’’, CRAN. <https://cran.rproject.org/web/packages/lhs/lhs.pdf>.
- Collins, G., Francom, D. & Rumsey, K. (2024), ‘Bayesian projection pursuit regression’, *Statistics and Computing* **34**(1), 29.
- Constantine, P. G. (2015), *Active subspaces: Emerging ideas for dimension reduction in parameter studies*, SIAM.
- Constantine, P. G. & Diaz, P. (2017), ‘Global sensitivity metrics from active subspaces’, *Reliability Engineering & System Safety* **162**, 1–13.
- Constantine, P. G. & Doostan, A. (2017), ‘Time-dependent global sensitivity analysis with active subspaces for a lithium ion battery model’, *Statistical Analysis and Data Mining: The ASA Data Science Journal* **10**(5), 243–262.
- Constantine, P. G., Zaharatos, B. & Campanelli, M. (2015), ‘Discovering an active subspace in a single-diode solar cell model’, *Statistical Analysis and Data Mining: The ASA Data Science Journal* **8**(5-6), 264–273.
- Constantine, P. & Gleich, D. (2014), ‘Computing active subspaces with monte carlo’, *arXiv preprint arXiv:1408.0545* .
- Cook, R. D. (2022), ‘A slice of multivariate dimension reduction’, *Journal of Multivariate Analysis* **188**, 104812.

- Crowley, W. (2005), Flag: A free-lagrange method for numerically simulating hydrodynamic flows in two dimensions, *in* 'Proceedings of the Second International Conference on Numerical Methods in Fluid Dynamics: September 15–19, 1970 University of California, Berkeley', Springer, pp. 37–43.
- Davison, L. & Stevens, A. (1972), 'Continuum measures of spall damage', *Journal of Applied Physics* **43**(3), 988–994.
- Denison, D. G., Mallick, B. K. & Smith, A. F. (1998), 'Bayesian MARS', *Statistics and Computing* **8**(4), 337–346.
- Dong, Y., Soale, A.-N. & Power, M. D. (2023), 'A selective review of sufficient dimension reduction for multivariate response regression', *Journal of Statistical Planning and Inference* **226**, 63–70.
- Finnegan, S., Haines, B., Haynes, D., Hoffman, N., Pruet, J., Vander Wiel, S. & Wilson, B. (2022), Report on the narrative uncertainty workshop, Technical Report LA-UR-23-22141, Los Alamos National Laboratory.
- Francom, D. & Sansó, B. (2020), 'Bass: An r package for fitting and performing sensitivity analysis of bayesian adaptive spline surfaces', *Journal of Statistical Software* **94**(1), 1–36.
- Francom, D., Sansó, B., Bulaevskaya, V., Lucas, D. & Simpson, M. (2019), 'Inferring atmospheric release characteristics in a large computer experiment using bayesian adaptive splines', *Journal of the American Statistical Association* **114**(528), 1450–1465.
- Francom, D., Sansó, B., Kupresanin, A. & Johannesson, G. (2018), 'Sensitivity analysis and emulation for functional data using bayesian adaptive splines', *Statistica Sinica* pp. 791–816.
- Fredenburg, D. A., Aslam, T. D. & Bennett, L. S. (2015), A grüneisen equation of state for tpx: Application in flag, Technical Report LA-UR-15-28533, Los Alamos National Laboratory.
- Friedman, J. H. (1991), 'Multivariate adaptive regression splines', *The annals of statistics* pp. 1–67.
- Golub, G. H. & Van Loan, C. F. (2013), *Matrix computations*, JHU press.
- Gramacy, R. B. (2020), *Surrogates: Gaussian process modeling, design, and optimization for the applied sciences*, CRC press.
- Hsing, T. (1999), 'Nearest neighbor inverse regression', *The Annals of Statistics* **27**(2), 697–731.
- Hutchings, G., Sansó, B., Gattiker, J., Francom, D. & Pasqualini, D. (2023), 'Comparing emulation methods for a high-resolution storm surge model', *Environmetrics* **34**(3), e2796.
- Ji, W., Ren, Z., Marzouk, Y. & Law, C. K. (2019), 'Quantifying kinetic uncertainty in turbulent combustion simulations using active subspaces', *Proceedings of the Combustion Institute* **37**(2), 2175–2182.

- Ji, W., Wang, J., Zahm, O., Marzouk, Y. M., Yang, B., Ren, Z. & Law, C. K. (2018), ‘Shared low-dimensional subspaces for propagating kinetic uncertainty to multiple outputs’, *Combustion and Flame* **190**, 146–157.
- Kennedy, M. C. & O’Hagan, A. (2001), ‘Bayesian calibration of computer models’, *Journal of the Royal Statistical Society: Series B (Statistical Methodology)* **63**(3), 425–464.
- Kruskal, J. B. (1964), ‘Nonmetric multidimensional scaling: a numerical method’, *Psychometrika* **29**(2), 115–129.
- Lawson, A. C. (2009), ‘Physics of the lindemann melting rule’, *Philosophical Magazine* **89**(22-24), 1757–1770.
- Lee, E., Hornig, H. & Kury, J. (1968), Adiabatic expansion of high explosive detonation products, Technical report, Univ. of California Radiation Lab. at Livermore, Livermore, CA (United States).
- Lee, M. R. (2019), ‘Modified active subspaces using the average of gradients’, *SIAM/ASA Journal on Uncertainty Quantification* **7**(1), 53–66.
- Li, B., Wen, S. & Zhu, L. (2008), ‘On a projective resampling method for dimension reduction with multivariate responses’, *Journal of the American Statistical Association* **103**(483), 1177–1186.
- Li, K.-C. (1991), ‘Sliced inverse regression for dimension reduction’, *Journal of the American Statistical Association* **86**(414), 316–327.
- Lin, J.-N. & Unbehauen, R. (1992), ‘Canonical piecewise-linear approximations’, *IEEE Transactions on Circuits and Systems I: Fundamental Theory and Applications* **39**(8), 697–699.
- Lukaczyk, T. W., Constantine, P., Palacios, F. & Alonso, J. J. (2014), Active subspaces for shape optimization, in ‘10th AIAA multidisciplinary design optimization conference’, p. 1171.
- Ma, Y. & Zhu, L. (2013), ‘A review on dimension reduction’, *International Statistical Review* **81**(1), 134–150.
- Mead, A. (1992), ‘Review of the development of multidimensional scaling methods’, *Journal of the Royal Statistical Society: Series D (The Statistician)* **41**(1), 27–39.
- Michelsen, H. A., Liu, F., Kock, B. F., Bladh, H., Boïarciuc, A., Charwath, M., Dreier, T., Hedef, R., Hofmann, M., Reimann, J. et al. (2007), ‘Modeling laser-induced incandescence of soot: a summary and comparison of lii models’, *Applied physics B* **87**, 503–521.
- Nott, D. J., Kuk, A. Y. & Duc, H. (2005), ‘Efficient sampling schemes for bayesian mars models with many predictors’, *Statistics and Computing* **15**(2), 93–101.
- Okabe, A., Boots, B., Sugihara, K. & Chiu, S. N. (2009), ‘Spatial tessellations: concepts and applications of voronoi diagrams’.

- Park, J.-S. (1994), ‘Optimal latin-hypercube designs for computer experiments’, *Journal of statistical planning and inference* **39**(1), 95–111.
- Peherstorfer, B., Willcox, K. & Gunzburger, M. (2018), ‘Survey of multifidelity methods in uncertainty propagation, inference, and optimization’, *Siam Review* **60**(3), 550–591.
- Rall, L. B. & Corliss, G. F. (1996), ‘An introduction to automatic differentiation’, *Computational Differentiation: Techniques, Applications, and Tools* **89**, 1–18.
- Rumsey, K., Francom, D. & Vander Wiel, S. (2023), ‘Discovering active subspaces for high-dimensional computer models’, *Journal of Computational and Graphical Statistics* pp. 1–13.
- Rumsey, K. N., Francom, D. & Shen, A. (2024), ‘Generalized bayesian mars: Tools for stochastic computer model emulation’, *SIAM/ASA Journal on Uncertainty Quantification* **12**(2), 646–666.
- Rumsey, K. N., Huerta, G. & Derek Tucker, J. (2023), ‘A localized ensemble of approximate gaussian processes for fast sequential emulation’, *Stat* **12**(1), e576.
- Seshadri, P., Shahpar, S., Constantine, P., Parks, G. & Adams, M. (2018), ‘Turbomachinery active subspace performance maps’, *Journal of Turbomachinery* **140**(4).
- Setodji, C. M. & Cook, R. D. (2004), ‘K-means inverse regression’, *Technometrics* **46**(4), 421–429.
- Steinberg, D., Cochran, S. & Guinan, M. (1980), ‘A constitutive model for metals applicable at high-strain rate’, *Journal of applied physics* **51**(3), 1498–1504.
- Stone, M. (1978), ‘Cross-validation: A review’, *Statistics: A Journal of Theoretical and Applied Statistics* **9**(1), 127–139.
- Tezzele, M., Ballarin, F. & Rozza, G. (2018), Combined parameter and model reduction of cardiovascular problems by means of active subspaces and pod-galerkin methods, in ‘Mathematical and numerical modeling of the cardiovascular system and applications’, Springer, pp. 185–207.
- Van Dongen, S. & Enright, A. J. (2012), ‘Metric distances derived from cosine similarity and pearson and spearman correlations’, *arXiv preprint arXiv:1208.3145* .
- Weseloh, W. N. (2014), Jwl in a nutshell, Technical Report LA-UR-14-24318, Los Alamos National Laboratory.
- Wycoff, N., Binois, M. & Wild, S. M. (2021), ‘Sequential learning of active subspaces’, *Journal of Computational and Graphical Statistics* **30**(4), 1224–1237.
- Yannotty, J. C., Santner, T. J., Furnstahl, R. J. & Pratola, M. T. (2024), ‘Model mixing using bayesian additive regression trees’, *Technometrics* **66**(2), 196–207.

- Ye, K. & Lim, L.-H. (2016), 'Schubert varieties and distances between subspaces of different dimensions', *SIAM Journal on Matrix Analysis and Applications* **37**(3), 1176–1197.
- Zacks, S. (1998), *Modern industrial statistics: design and control of quality and reliability*, Cengage Learning.
- Zahm, O., Constantine, P. G., Prieur, C. & Marzouk, Y. M. (2020), 'Gradient-based dimension reduction of multivariate vector-valued functions', *SIAM Journal on Scientific Computing* **42**(1), A534–A558.
- Zhang, W. & Zhang, W. (2020), 'A review of surrogate models', *MARS Applications in Geotechnical Engineering Systems: Multi-Dimension with Big Data* pp. 7–17.

Supplemental Materials

SM1 Additional Details on Rate Stick Experiment Diagnostics

This brief section goes into additional details regarding the simulated PDV probes. PDV probes function by measuring the reflected light from a laser directed at a surface. When the surface is moving, this will result in a small shift in the the laser frequency, which can be directly related to the velocity of the surface.

In each of the simulations, five different PDV probes were modeled with equidistant axial spacing. Computationally, the probes are defined with by their origin and laser direction. The probes are defined 3.9 cm from the outer metal jacket surface (5 cm from the origin) with 1.6 cm axial spacing, and are directed along the radial axial (directly at the outer surface).

Figure 8 shows the time-dependent PDV data for each of the probes. The initial rise in the velocity profiles

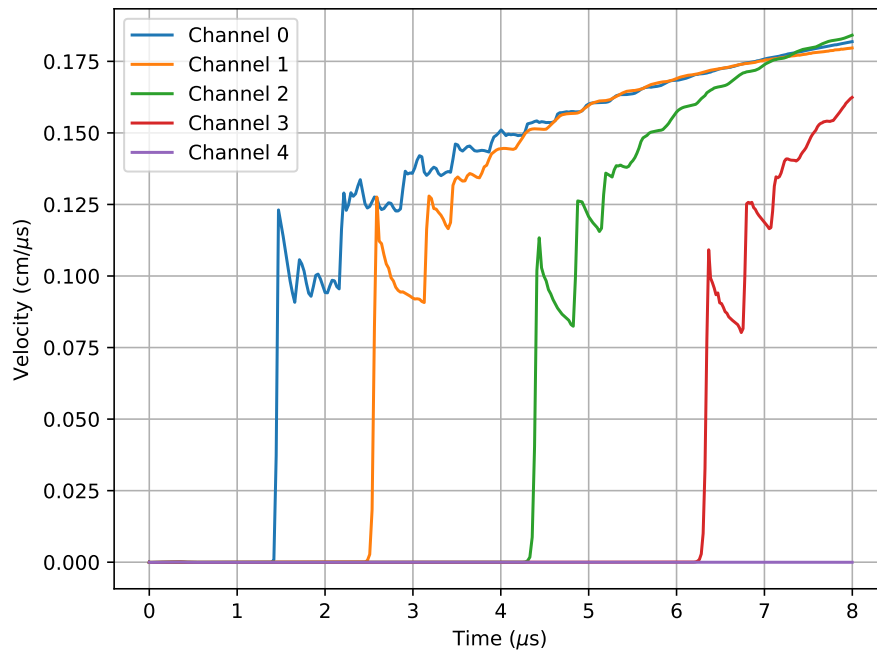


Figure 8: The PDV signal from a nominal rate stick experiment with a copper jacket.

indicates the arrival time of the shock at the outer boundary of the problem at the respective probe elevations. From the spacing in the shock arrival times, it is clear that the speed of the detonation front changes throughout the simulation. Once the detonation front passes channel 1, the detonation speed remains rela-

tively constant, indicating the detonation front has reached its steady burn rate. This characteristic provided the primary rationale in choosing to analyze PDV measurements at later times and higher axial positions.

Several more important features can be taken from Figure 8. The velocity profiles exhibit quite complex behaviors. Once the initial shock has reached the outer surface of the metal jacket, a rarefaction wave is reflected back into the jacket. This leads to the subsequent decrease in velocity. The remaining behaviors are explained by the shocks “ringing” in the system. Each time a shock reaches an interface, part of it is transmitted to the neighboring material, and part is reflected as either a shock or rarefaction wave. As time goes on, the strength of the shock is attenuated, but many more wave fronts exist for a give elevation. This leads to the velocity profiles smoothing out over time. Because the aim was to compare the concordance of different metal jackets, it was important to choose a measurement far enough away from the shock front arrival time to capture the integral material response for comparison.

SM2 Discordance as a pseudo-metric

A pseudo-metric is a metric but without requiring the identity of indiscernibles, meaning two objects with zero distance are necessarily the same. This section demonstrates that discordance defined in Eq. (10) is a pseudo-metric. Functions f_1, f_2, \dots are taken to have inputs \mathbf{x} . Discordance is defined as

$$\text{discord}(f_k, f_\ell) = \sqrt{\frac{1 - \text{conc}(f_k, f_\ell)}{2}}, \quad (27)$$

with concordance defined in Eq. (9).

The four properties of a pseudo metric are:

non-negative: $d(f_k, f_\ell) \geq 0$ follows from $\text{conc}(f_k, f_\ell) \in [-1, 1]$.

zero self-distance: $d(f_k, f_k) = 0$ follows from Eq. (9) and (10) by recalling that $t_{kk} = t_k$ so $\text{conc}(f_k, f_k) = 1$.

symmetry: $d(f_k, f_\ell) = d(f_\ell, f_k)$ follows from Eq. (9) by noting from Eq. (5) that $t_{k\ell} = t_{\ell k}$

The final property is the **triangle inequality**

$$d(f_k, f_\ell) \leq d(f_k, f_m) + d(f_m, f_\ell)$$

which requires a little work. For an i.i.d. sample $\mathbf{x}_1, \mathbf{x}_2, \dots \sim \mu$ the Strong Law of Large Numbers gives

$$t_{k\ell}^{(L)} \equiv L^{-1} \sum_{m=1}^L \nabla f_k(\mathbf{x}_m)^\top \nabla f_\ell(\mathbf{x}_m) \xrightarrow{\text{a.s.}} E_\mu [\nabla f_k(\mathbf{x})^\top \nabla f_\ell(\mathbf{x})] = t_{k\ell} \quad (28)$$

as $L \rightarrow \infty$. Define the vector

$$\mathbf{z}_{kL} = (\nabla f_k(\mathbf{x}_1)^\top, \dots, \nabla f_k(\mathbf{x}_L)^\top)^\top$$

so that (assuming gradients are not a.s. zero)

$$\kappa_{k\ell}^{(L)} \equiv \frac{\mathbf{z}_{kL}^\top \mathbf{z}_{\ell L}}{\sqrt{(\mathbf{z}_{kL}^\top \mathbf{z}_{kL}) (\mathbf{z}_{\ell L}^\top \mathbf{z}_{\ell L})}} = \frac{t_{k\ell}^{(L)}}{\sqrt{t_{kk}^{(L)} t_{\ell\ell}^{(L)}}} \xrightarrow{\text{a.s.}} \frac{t_{k\ell}}{\sqrt{t_{kk} t_{\ell\ell}}} = \text{conc}(f_k, f_\ell). \quad (29)$$

Thus, if $\sqrt{1 - c_{k\ell}^{(L)}}$ obeys the triangle inequality, then so does $\text{discord}(\cdot, \cdot)$. The definition of $c_{k\ell}^{(L)}$ in Equation (29) shows it as the cosine of the angle between \mathbf{z}_{kL} and $\mathbf{z}_{\ell L}$ and (Van Dongen & Enright 2012, Sec. 4) proves that $\sqrt{1 - c}$ obeys the triangle inequality when c is the cosine of the angle between Euclidean vectors.

□

SM3 Details for efficient approximation of the co-Constantine matrix

With slightly more generality than in the main text, suppose that $f^{(k)}(\mathbf{x})$ can be written as

$$f_k(\mathbf{x}) \approx \gamma_{k0} + \sum_{m=1}^{M_k} \gamma_{km} \prod_{i=1}^p h_{im}^{(k)}(x_i), \quad (30)$$

In this setting, the univariate integrals (from Eq. (23)) that we need to compute can be written as

$$\begin{aligned} I_{1,k\ell}^{(i)}[m_1, m_2] &= \int_{-\infty}^{\infty} \frac{dh_{im_1}^{(k)}(x)}{dx} h_{im_2}^{(\ell)}(x) \mu_i(x) dx \\ I_{2,k\ell}^{(i)}[m_1, m_2] &= \int_{-\infty}^{\infty} h_{im_1}^{(k)}(x) h_{im_2}^{(\ell)}(x) \mu_i(x) dx \\ I_{3,k\ell}^{(i)}[m_1, m_2] &= \int_{-\infty}^{\infty} \frac{dh_{im_1}^{(k)}(x)}{dx} \frac{dh_{im_2}^{(\ell)}(x)}{dx} \mu_i(x) dx. \end{aligned} \quad (31)$$

It is important to note that $I_{r,k\ell}^{(i)}$ and $I_{r,\ell k}^{(i)}$ are the same for $r = 2$ and $r = 3$, but these quantities must be computed separately for $r = 1$. Additionally, none of the matrices are likely to be symmetric (or even

square). This why (for $M = M_1 = M_2$) there are $4pM^2$ univariate integrals to compute here, compared to just $pM(2M - 1)$ integrals in the single function case explored by Rumsey, Francom & Vander Wiel (2023).

In the case where Equation (30) is a MARS model (as is the case for the `concordance R` package), we have

$$h_{im}^{(k)}(x_i) = [\chi_{kim}(x_i) s_{kim}(x_i - t_{kim})]^{u_{kim}}$$

and

$$\frac{d}{dx_i} h_{im}^{(k)}(x_i) = u_{kim} s_{kim} \chi_{kim}(x_i)$$

where $\chi_{kim}(x) = \mathbb{1}(s_{kim}(x_i - t_{kim}) > 0)$. Thus, to compute the integrals above for this special case, we only need to evaluate truncated moments (with respect to μ_i) of order $r \in \{0, 1, 2\}$

$$\xi(r|a, b, \mu_i) = \int_a^b x^r \mu_i(x) dx.$$

From here, letting $\xi(r)$ denote $\xi(r|a_{k\ell}^{(i)}[m_1, m_2], b_{k\ell}^{(i)}[m_1, m_2], \mu_i)$, it is straightforward to show that

$$I_{1,k\ell}^{(i)}[m_1, m_2] = s_{kim_1} s_{\ell im_2} \begin{cases} u_{kim_1} (\xi(1) - t_{\ell im_2} \xi(0)), & u_{\ell im_2} = 1 \\ u_{kim_1} \xi(0), & u_{\ell im_2} = 0 \end{cases} \quad (32)$$

$$I_{2,k\ell}^{(i)}[m_1, m_2] = s_{kim_1} s_{\ell im_2} \begin{cases} \xi(2) - (t_{kim_1} + t_{\ell im_2}) \xi(1) + t_{kim_1} t_{\ell im_2} \xi(0), & u_{kim_1} = 1, u_{\ell im_2} = 1 \\ \xi(1) - t_{kim_1} \xi(0), & u_{kim_1} = 1, u_{\ell im_2} = 0 \\ \xi(1) - t_{\ell im_2} \xi(0), & u_{kim_1} = 0, u_{\ell im_2} = 1 \\ 1, & u_{kim_1} = 0, u_{\ell im_2} = 0 \end{cases} \quad (33)$$

$$I_{3,k\ell}^{(i)}[m_1, m_2] = u_{kim_1} u_{\ell im_2} s_{kim_1} s_{\ell im_2} \xi(0). \quad (34)$$

The bounds, $a_{k\ell}^{(i)}[m_1, m_2], b_{k\ell}^{(i)}[m_1, m_2], \mu_i$, are given by

$$\begin{aligned}
 a_{k\ell}^{(i)}[m_1, m_2] &= \begin{cases} \max(t_{kim_1}, t_{lim_2}), & s_{kim_1} = +1, s_{lim_2} = +1 \\ t_{kim_1}, & s_{kim_1} = +1, s_{lim_2} = -1 \\ t_{lim_2}, & s_{kim_1} = -1, s_{lim_2} = +1 \\ -\infty, & s_{kim_1} = -1, s_{lim_2} = -1 \end{cases} \\
 b_{\star, k\ell}^{(i)}[m_1, m_2] &= \begin{cases} \infty, & s_{kim_1} = +1, s_{lim_2} = +1 \\ t_{lim_2}, & s_{kim_1} = +1, s_{lim_2} = -1 \\ t_{kim_1}, & s_{kim_1} = -1, s_{lim_2} = +1 \\ \min(t_{kim_1}, t_{lim_2}), & s_{kim_1} = -1, s_{lim_2} = -1 \end{cases} \quad (35) \\
 b_{k\ell}^{(i)}[m_1, m_2] &= \max \left\{ b_{\star, k\ell}^{(i)}[m_1, m_2], a_{k\ell}^{(i)}[m_1, m_2] \right\}.
 \end{aligned}$$

This has been implemented in the `concordance` package. R code to conduct a simple toy analysis is given below.

```

#install.packages("BASS")
#devtools::install_github("knumsey/concordance")
f <- function(x, scale=0) x[1]^2 + x[1]*x[2] + x[2]^3*scale
X <- matrix(runif(300), ncol=3)
y1 <- apply(X, 1, f)
y2 <- apply(X, 1, f, scale=1/2)
mod1 <- BASS::bass(X, y1)
mod2 <- BASS::bass(X, y2)
C <- concordance::Cfg_bass(mod1, mod2)

```

3.1 The Modified Co-ASM

To compute the modified Co-ASM as suggested by Lee (2019) for quadratic functions (see Eq. (9) in the main text), we need to be able to compute the expected gradient

$$Z_k = E[\nabla f_k(\mathbf{x})]. \quad (36)$$

Using the same infrastructure as the above, we can write that

$$E \left[\frac{\partial f_k(\mathbf{x})}{\partial x_i} \right] = \sum_{m=1}^M \gamma_m I_{4,k}^{(i)}[m] \prod_{j \neq i} I_{5,k}^{(i)}[m]. \quad (37)$$

where $I_{4,k}^{(i)}[m] = \int_{-\infty}^{\infty} h^{(k)'}_{im}(x) \mu_i(x) dx$ and $I_{5,k}^{(i)}[m] = \int_{-\infty}^{\infty} h^{(k)}_{im}(x) \mu_i(x) dx$. In the case of MARS, these integrals are given by

$$\begin{aligned} I_{4,k}^{(i)}[m] &= s_{kim} u_{kim} \xi(0|a_{kim}, b_{kim}, \mu_i) \\ I_{5,k}^{(i)}[m] &= (s_{kim} (\xi(1|a_{kim}, b_{kim}, \mu_i) - t_{kim}) \xi(0|a_{kim}, b_{kim}, \mu_i))^{u_{kim}} \\ a_{kim} &= \frac{2s_{kim} t_{kim}}{s_{kim} + 1} \\ b_{kim} &= \frac{2s_{kim} t_{kim}}{s_{kim} - 1}, \end{aligned} \quad (38)$$

where $a_{kim}, b_{kim} \in \mathbb{R} \cup \{-\infty, \infty\}$. The expected gradient vector can be computed with the concordance package as

```
#install.packages("BASS")
#devtools::install_github("knumsey/concordance")
f <- function(x, scale=0) x[1]^2 + x[1]*x[2] + x[2]^3*scale
X <- matrix(runif(300), ncol=3)
y1 <- apply(X, 1, f)
mod1 <- BASS::bass(X, y1)
Z <- concordance::Z_bass(mod1)
```

An example can be found at `inst/CoASM/Z_bass_example.R` in the github repo.

3.2 Pseudocode

Pseudo code for estimating the co-Constantine matrix C_{12} for functions f_1 and f_2 . The inputs to the algorithm include a set of inputs $\mathbf{x}_1, \dots, \mathbf{x}_n$ and two sets of outputs $y_{1i} = f_1(\mathbf{x}_i)$ and $y_{2i} = f_2(\mathbf{x}_i)$

for $i = 1, \dots, n$. We also have to specify the (marginally independent) prior for each input μ_1, \dots, μ_p .

Algorithm 1: Pseudocode for the computation of the co-constantine matrix C_{ij} . We use the notation

\mathcal{M} .field to denote a “field” or “attribute” belonging to object (model) \mathcal{M} .

Input: $(\mathbf{x}_1, y_{11}, y_{21}), \dots, (\mathbf{x}_n, y_{1n}, y_{2n}), \mu_1, \dots, \mu_p$

Output: Co-Constantine matrix: C

$\mathcal{M}_1 \leftarrow \text{BASS}(\{\mathbf{x}_1, \dots, \mathbf{x}_n\}, \{y_{11}, \dots, y_{1n}\});$ // Fit emulators with Francom & Sansó
(2020)

$\mathcal{M}_2 \leftarrow \text{BASS}(\{\mathbf{x}_1, \dots, \mathbf{x}_n\}, \{y_{21}, \dots, y_{2n}\})$

Initialize: $a, b, I_1, I_2, I_3 \in \mathbb{R}^{(\mathcal{M}_1.M) \times (\mathcal{M}_2.M) \times p}$

for $m_1 \leftarrow 1$ **to** $\mathcal{M}_1.M$ **do**

for $m_2 \leftarrow 1$ **to** $\mathcal{M}_2.M$ **do**

for $i \leftarrow 1$ **to** p **do**

 params $\leftarrow (\mathcal{M}_1.s, \mathcal{M}_1.t, \mathcal{M}_1.u, \mathcal{M}_2.s, \mathcal{M}_2.t, \mathcal{M}_2.u)$

Compute $a^{(i)}[m_1, m_2](\text{params});$ // Equation (35)

Compute $b^{(i)}[m_1, m_2](\text{params});$ // Equation (35)

Compute $I_1^{(i)}[m_1, m_2](\text{params}, a^{(i)}[m_1, m_2], b^{(i)}[m_1, m_2], \mu_i);$ // Equation (32)

Compute $I_2^{(i)}[m_1, m_2](\text{params}, a^{(i)}[m_1, m_2], b^{(i)}[m_1, m_2], \mu_i);$ // Equation (33)

Compute $I_3^{(i)}[m_1, m_2](\text{params}, a^{(i)}[m_1, m_2], b^{(i)}[m_1, m_2], \mu_i);$ // Equation (34)

end

end

end

Initialize C_{12}

for $i \leftarrow 1$ **to** p **do**

for $j \leftarrow 1$ **to** p **do**

Compute $C_{12}[i, j](I_1, I_2, I_3, \mathcal{M}_1.\text{coeff}, \mathcal{M}_2.\text{coeff});$ // Equation (25) in main

 text

end

end

Return C_{ij}

SM4 Numerical study with Piston function

In this example, we demonstrate the correctness of the numerical method proposed in the main manuscript by comparing the result to a Monte Carlo based approach. In most practical problems, the MC based approach suffers from limitations, as described in the main problem. Here, we use a simple analytic example for which the MC approach can be computed reasonably quickly, and thus the MC approximation for C_{12} is used as ground truth.

Consider the *Piston function* (Zacks 1998, Ben-Ari & Steinberg 2007), traditionally defined as

$$f(\mathbf{x}) = 120\pi \sqrt{\frac{M}{k + S^2 \frac{P_0 V_0 T_a}{T_0 V^2}}}, \quad \text{where} \quad (39)$$

$$V = \frac{S}{2k} \left(\sqrt{A^2 + 4k \frac{P_0 V_0 T_a}{T_0}} - A \right) \quad \text{and} \quad A = P_0 S + 19.62M - \frac{kV_0}{S},$$

with standard parameter ranges given in Table 6. We consider modeling the piston function for two different settings of the ambient conditions. The table indicates the $p = 5$ global simulation variables (x_1, \dots, x_5) and the simulation variables ξ_1, ξ_2 . We define two computer models as

$$f_1(\mathbf{x} | \xi_1 = 90000, \xi_2 = 284) \quad (40)$$

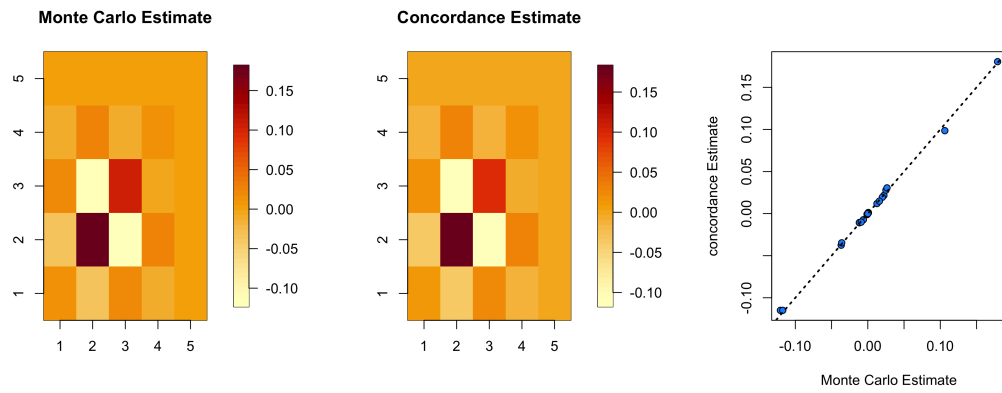
$$f_2(\mathbf{x} | \xi_1 = 110000, \xi_2 = 302),$$

where the inputs \mathbf{x} are scaled to $[0, 1]^5$ for simplicity. The matrix C_{12} is first estimated using a highly-accurate MC approach with $M = 100,000$ draws and using forward automatic differentiation (Rall & Corliss 1996) for gradient estimation (using the `fd_grad()` function in the `concordance` package). For comparison, we also estimate the C_{12} matrix using the method described in Section 3.4 of the main manuscript (using

notation	input	range	description
x_1	M	[30, 60]	piston weight (kg)
x_2	S	[0.005, 0.020]	piston surface area (m^2)
x_3	V_0	[0.002, 0.010]	initial gas volume (m^3)
x_4	k	[1000, 5000]	spring coefficient (N/m)
x_5	T_0	[340, 360]	filling gas temperature (K)
ξ_1	P_0	[90000, 110000]	atmospheric pressure (N/m^2)
ξ_2	T_a	[290, 296]	ambient temperature (K)

Table 6: Description of input variables and their ranges for the piston simulation function.

the `C_bass` function in the `concordance` package). R code to reproduce this example can be found at http://github.com/knrumsey/concordance/inst/CoASM/piston_coactive.R.



(a) Monte Carlo estimate of C_{12} for the piston functions. (b) Concordance package estimate of C_{12} for the piston functions. (c) Comparison of C_{12} entries for both estimation procedures.

Figure 9: Estimation of C_{12} for the piston functions.

SM5 PBX 9501 - Concordance Values

The following tables give the posterior mean and posterior standard deviations for the concordance analysis of the 14 different materials for the HE application in the main text.

Table 7: Concordance posterior mean

	copper	tungsten	ss304	gold	gold_5cu	uranium_5mo	nickel
copper	0.987	0.969	0.979	0.915	0.934	0.930	0.981
tungsten	0.969	0.998	0.981	0.940	0.953	0.942	0.984
ss304	0.979	0.981	1.000	0.930	0.946	0.938	0.996
gold	0.915	0.940	0.930	0.991	0.880	0.888	0.927
gold_5cu	0.934	0.953	0.946	0.880	0.999	0.887	0.951
uranium_5mo	0.930	0.942	0.938	0.888	0.887	0.998	0.941
nickel	0.981	0.984	0.996	0.927	0.951	0.941	0.999
uranium_075ti	0.930	0.946	0.945	0.869	0.935	0.944	0.949
al6061	0.962	0.958	0.982	0.906	0.918	0.913	0.981
uranium	0.899	0.931	0.918	0.859	0.954	0.820	0.921
ss250	0.976	0.978	0.995	0.933	0.944	0.934	0.992
tin	0.965	0.947	0.972	0.899	0.925	0.904	0.973
ss4340	0.978	0.980	0.999	0.931	0.945	0.937	0.996
al7075	0.965	0.960	0.984	0.907	0.920	0.915	0.983

	uranium_075ti	al6061	uranium	ss250	tin	ss4340	al7075
copper	0.930	0.962	0.899	0.976	0.965	0.978	0.965
tungsten	0.946	0.958	0.931	0.978	0.947	0.980	0.960
ss304	0.945	0.982	0.918	0.995	0.972	0.999	0.984
gold	0.869	0.906	0.859	0.933	0.899	0.931	0.907
gold_5cu	0.935	0.918	0.954	0.944	0.925	0.945	0.920
uranium_5mo	0.944	0.913	0.820	0.934	0.904	0.937	0.915
nickel	0.949	0.981	0.921	0.992	0.973	0.996	0.983
uranium_075ti	0.995	0.921	0.885	0.940	0.923	0.943	0.922
al6061	0.921	0.999	0.894	0.977	0.964	0.982	0.999
uranium	0.885	0.894	1.000	0.920	0.890	0.918	0.895
ss250	0.940	0.977	0.920	0.999	0.971	0.995	0.979
tin	0.923	0.964	0.890	0.971	0.999	0.971	0.965
ss4340	0.943	0.982	0.918	0.995	0.971	0.999	0.984
al7075	0.922	0.999	0.895	0.979	0.965	0.984	1.000

Table 8: Concordance posterior standard deviations

	copper	tungsten	ss304	gold	gold_5cu	uranium_5mo	nickel
copper	0.006	0.003	0.004	0.010	0.006	0.006	0.004
tungsten	0.003	0.002	0.001	0.011	0.005	0.005	0.002
ss304	0.004	0.001	0.0005	0.010	0.005	0.005	0.002
gold	0.010	0.011	0.010	0.011	0.011	0.010	0.010
gold_5cu	0.006	0.005	0.005	0.011	0.002	0.007	0.005
uranium_5mo	0.006	0.005	0.005	0.010	0.007	0.004	0.006
nickel	0.004	0.002	0.002	0.010	0.005	0.006	0.001
uranium_075ti	0.007	0.006	0.006	0.011	0.007	0.009	0.006
al6061	0.004	0.001	0.001	0.010	0.005	0.005	0.002
uranium	0.005	0.004	0.004	0.010	0.007	0.005	0.004
ss250	0.003	0.001	0.001	0.010	0.005	0.005	0.002
tin	0.005	0.004	0.004	0.010	0.006	0.006	0.004
ss4340	0.003	0.001	0.001	0.010	0.005	0.005	0.002
al7075	0.004	0.001	0.001	0.010	0.005	0.005	0.002

	uranium_075ti	al6061	uranium	ss250	tin	ss4340	al7075
copper	0.007	0.004	0.005	0.003	0.005	0.003	0.004
tungsten	0.006	0.001	0.004	0.001	0.004	0.001	0.001
ss304	0.006	0.001	0.004	0.001	0.004	0.001	0.001
gold	0.011	0.010	0.010	0.010	0.010	0.010	0.010
gold_5cu	0.007	0.005	0.007	0.005	0.006	0.005	0.005
uranium_5mo	0.009	0.005	0.005	0.005	0.006	0.005	0.005
nickel	0.006	0.002	0.004	0.002	0.004	0.002	0.002
uranium_075ti	0.005	0.006	0.006	0.006	0.007	0.006	0.006
al6061	0.006	0.001	0.004	0.001	0.003	0.001	0.001
uranium	0.006	0.004	0.001	0.004	0.005	0.004	0.004
ss250	0.006	0.001	0.004	0.001	0.003	0.001	0.001
tin	0.007	0.003	0.005	0.003	0.003	0.004	0.003
ss4340	0.006	0.001	0.004	0.001	0.004	0.001	0.001
al7075	0.006	0.001	0.004	0.001	0.003	0.001	0.000